Applying desktop GPUs to a hybrid ABM and PDM: model validation and rapid simulation of viral infections

APPLYING DESKTOP GPUS TO A HYBRID ABM AND PDM: MODEL VALIDATION AND RAPID SIMULATION OF VIRAL INFECTIONS

by

BAYLOR G. FAIN

Bachelor of Science, 2016
Tarleton State University
Stephenville, Texas

Submitted to the Graduate Faculty of the
College of Science and Engineering
Texas Christian University
in partial fulfillment of the requirements
for the degree of

Masters of Science

Aug 2021

ACKNOWLEDGMENTS

Studying viruses during a pandemic gives a person a different view of the effects occurring worldwide. It shows you how making your research accessible to all people is so very important. I'm truly thankful to all the doctors, nurses, educators, and researchers who worked even when at risk of becoming sick. For me specifically, I must thank my wife, Kelli, for not only helping me manage during the transition time of being only at home, but also for being a mentor of writing. I must also thank my advisor Dr. Dobrovolny, for not giving up on me even when I thought I could not continue, checking on me when I need it, and for bringing me back on track when I venture off with small details or a side project. Thank you to my mom Sharon, my first physics teacher, for introducing me to physics, believing in me, and giving me new recipes to try during the stay at home time. Thank you to my committee for agreeing to review my work, to ensure it is of the necessary quality.

Contents

List of Figures

List of Tables

List of Abbreviations

ABM	Agent based model
API	Application Programming Interface
AUC	Area under the curve
COVID-19	Coronavirus Disease 2019
CPU	Central Processing Unit
CUDA	Compute Unified Device Architecture
ET	Eclipse time
GPU	Graphics Processing Unit
HT	Healthy time
IT	Infected time
MOI	Multiplicity of Infection
MDCK	Madin-Darby canine kidney
ODE	Ordinary differential equation
PDE	Partial differential equation
PDM	Partial differential equation model
PFU	Plaque Forming Unit
RAM	Random Access Memory
RNA	Ribonucleic acid
SARS-CoV-2	Severe Acute Respiratory Syndrome Coronavirus 2
SSR	Sum of square residuals
STD	Standard Deviation
$TCID_{50}$	50% Tissue Culture Infectious Dose
UT	Universal time

Chapter 1

Introduction

The Coronavirus Disease 2019 (COVID-19) pandemic indicates how great of a need there is for accurate and fast modeling methods. In this thesis, I describe a model that incorporates the spatial spread of viruses and produces accurate simulations in a few seconds or minutes, so that the model can be used to study viruses in a more accurate way.

1.1 Basic Virology

Viruses are microscopic parasites, generally much smaller than bacteria, that lack the capacity to thrive and reproduce outside of a host body. A virus is composed of a nucleic acid genome and a protein capsid that covers the genome. As seen in figure 1.1, the life cycle of a virus begins with the virus attaching to or being absorbed by the host cell. Once the virus genome enters into a cell, the genome moves to the ribosomes, where the genome is replicated. After the genome is replicated, new virus can be assembled and

released from the host cell, allowing the virus to continue spreading throughout the host cells (OpenStax et al. 2016).

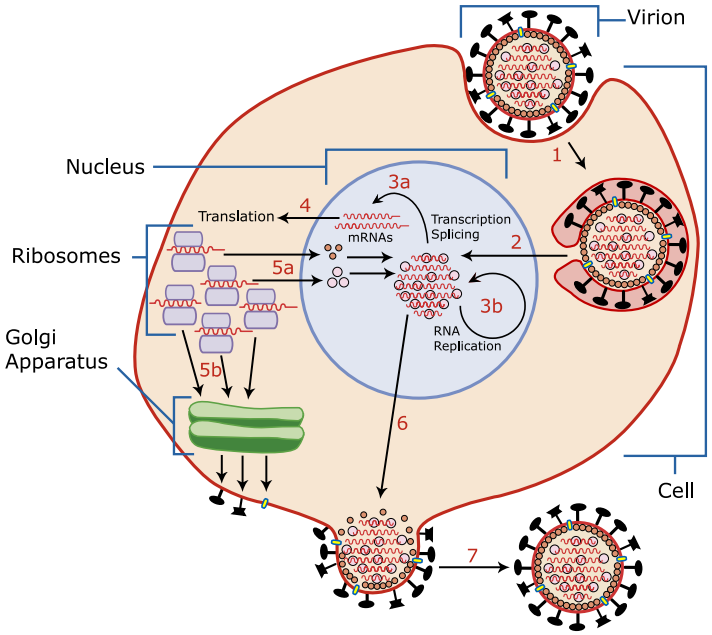

Figure 1.1: The life cycle of a virus begins with a virion (virus particle) being absorbed by the cell. Once the virion enters into a cell the virus genome is released. The genome moves to the ribosomes, where the genome is replicated. With the replicated genome, new virus can be assembled by the golgi apparatus and then released from the cell.

Some viruses cause illnesses and the spread of a few has been severe enough to cause global pandemics (global outbreaks). Recent examples are the current 2019-2021 Covid-19 pandemic, the 2014 Ebola pandemic, and the 2009 Swine Flu pandemic. Other viruses are endemic (regional outbreak) or occur seasonally (yearly outbreaks); for example, influenza (flu) is know for its spread each year in the United States. In total, the Centers for Disease Control and Prevention estimates that in the United States up to 42.9 million people were sick during the 2018-2019 flu season, 647,000 people were hospitalized, and 61,200 died. (Xu 2019)

In order to understand viruses, assays are performed. An assay is an experiment for

assessing or measuring characteristics of a substance. There are two ways the assays are carried out, *in vitro* or *in vivo*. *In vitro* assays are assays that are performed outside of a living organism. In virology, the plaque assay is the type of *in vitro* assay that is most widely used for determining viral titer (Pankaj 2021). These assays are often performed on a monolayer of cells in petri dishes or multi-well plates with a small number of wells. The dishes and plates are a type of adherent culture where the cells are grown on a nutritious substrate. The cells are grown to cover the entire surface (the point of confluence), at this point the cells tend to push on each other and distort the shape of each cell membrane (Brückner and Janshoff 2018). Each dish/well has on the order of 10^5–10^6 cells grown on its surface (Thermofisher). When the assay is performed, virus is placed in a dish/well of healthy cells. Any virus that causes damage to the cells in the dish/well can be studied. This damage is called a plaque and is roughly circular in shape. During the assay, formation of plaques and the concentration of virus are monitored. It is assumed that each plaque formed is caused by one virus particle. Because of this assumption, the viral concentration is often recorded as plaque forming units per milliliter (PFU/mL).

In vivo assays are assays that are performed in a multi-cellular living organism. Any virus that will infect the target animal can be studied. When the assay is performed, virus is introduced to the target animal through a nasal spray or injection. Then during the assay any visible symptoms and viral concentration are monitored.

1.2 Modeling of assays

In recent years, the field of virology has started using agent-based models to study the spread of viruses during *in vitro* viral infection assays (Beauchemin et al. 2005, Alvarado et al. 2018, Wodarz et al. 2014, Tong et al. 2015, Whitman et al. 2020, Goyal and Murray 2016, Itakura et al. 2010, Wasik et al. 2014) in an effort to study the spatiality of viral spread. The agent-based model framework is appealing to virus modelers because it allows for the individual tracking of how cells, as agents, interact with the virus, and has the potential to replicate *in vitro* and eventually *in vivo* viral infections.

Agent-based (individual-based or micro-simulation) models have been around since 1970 with the introduction of "Conway's Game of Life" (Gardner 1970). These models have been utilized in many different fields from physics to the study of fish (ichthyology) (Owusu et al. 2020) and continue to be popularized for different applications by software like Netlogo (Nogare and Chitnis 2020, Chiacchio et al. 2014). The models consist of a collection of agents whose behavior is determined by mathematical or computational rules. The agents of the system can move freely (Beauchemin et al. 2007) or be fixed in a grid or lattice (Beauchemin et al. 2005) for varying applications, but either configuration allows for tracking of spatially emergent patterns. To date, unfortunately, the implementation of agent-based models for simulating viral infections has had two issues: speed and size.

Agent-based models are notorious for being computationally intensive and taking long amounts of time to run simulations. This point has been commented on in a review of spatiotemporal models of viral infection (Gallagher et al. 2018), and the feasibility of

agent-based models for viral infection research has been talked about as a goal that is to come with increasing computational advancements (Bauer et al. 2009). Previous research has addressed this lack of computing power issue by reducing the number of agents modeled and therefore reducing the number of computations required for a simulation. The number of agents published is at minimum an order of magnitude lower than the number of target cells used in the corresponding experimental data. Beauchemin et al. (Beauchemin et al. 2005) simulated 1.232×10^5 agents, while the experiment they were attempting to replicate was performed in 6 well-plates and had $\sim 1.2 \times 10^6$ cells per well. Alvarado et al. (Alvarado et al. 2018) simulated 4.0×10^4 agents when trying to replicate experiments also performed in 6 well-plates. Wodarz et al. (Wodarz et al. 2014) simulated 2.0×10^4 agents, while the experiment they were replicating was performed in 24 well-plates and had $\sim 2.4 \times 10^5$ cells per well. Tong et al. (Tong et al. 2015) simulated 6.0×10^5 agents in an effort to simulate mice lungs, which have $\sim 10^9$ cells. These smaller simulations are more affected by boundary interactions, which can result in model dynamics that don't faithfully reproduce the infection. Having an in-host model that can produce accurate simulations in a timely manner not only allows for the prediction of patient infection, but also can be used to flush out potential causes of varying symptoms in patients.

1.3 Exigence

While it might be feasible to wait long periods of time to run accurate simulations for endemic or recurrent seasonal viruses, recent events of the COVID-19 pandemic indicate

how great a need there is for accurate and fast modeling methods. Epidemiological population-level modeling tools that include both ordinary differential equation models (Li et al. 2020, Ngonghala et al. 2020) and agent-based models (Ying and O'Clery 2021, Sneppen et al. 2021, Kano et al. 2021) were immediately deployed to help predict how the new virus would spread around the world and how different interventions could help stem the spread. At the within-host level, the primary modeling tool was limited to simple ordinary differential equation models (Gonçalves et al. 2020, Wang et al. 2020, Hernandez-Vargas and Velasco-Hernandez 2020, Dogra et al. 2020) that lack the ability to reproduce the spatial heterogeneity of real viral infections. Fast and accurate in-host models could be helpful in assessing the potential of re-purposed drugs (Czuppon et al. 2021, Gonçalves et al. 2020, Dodds et al. 2020), finding indicators of disease severity or mortality (Nant et al. 2021), and assessing the effectiveness of testing (Ejima et al. 2021). A community-driven agent-based model incorporating many realistic biological responses was quickly developed for Severe Acute Respiratory Syndrome Coronavirus 2 (SARS-CoV-2) (Getz et al. 2021), but is only currently simulating a few thousand agents and is expected to need high-performance computing or cloud resources to parameterize the model. Thus, there is a need to develop modeling and simulation tools for accurately predicting in-host viral dynamics that can be quickly deployed to help combat the next pandemic.

1.4 Scope

In this work, the testing, validation, and application of a hybrid agent-based model and partial differential equation model implemented on graphics processing units is presented. The work here begins with the methods where the four attributes of the model: (1) the agent-based model of the cells, (2) the partial differential equation of the virus, (3) the cell-free transmission mode of viruses, and (4) fitting of the model to data, are explained. Then, the results of model implementation with parallel programming, convergence testing, and simulation speed improvement are presented. Finally, I show that the model can reproduce experiments by fitting the model to an *in vitro* influenza virus experiment and an *in vitro* SARS-Cov-2 experiment. This work shows how an agent-based and partial differential equation hybrid model of in-host infections is tested for numerical convergence, is applied to experimental data for parameter extraction, and produces simulations within seconds to minutes for timely application.

Chapter 2

Methods

When studying something like viruses, that can have a huge effect on a person let alone a society, it is crucial to produce accurate simulations quickly. In the previous chapter, I showed how the field of virology has tried to use agent-based models to capture the spatial spread of viruses, but does not have either the computing power or coding tools to make the agent-based models feasible. In this chapter, a model for studying virus that incorporates the physics of viral spread both quickly and accurately is given in detail. I will present how the model accounts for spatial spread of virus, is able to produce simulations without compromising on accuracy, and can be applied to real experimental data.

2.1 Model details

In this work, a two dimensional biological system is simulated with a mathematical model. The system is a culture dish of a monolayer of cells with virus diffusing over the cells.

The model is a hybrid of an agent based model (ABM) and a partial differential equation model (PDM) where the cells are represented with an ABM and the virus diffusion is represented by a PDM.

2.1.1 Spatial accounting

To allow for the two dimensional aspect of the culture dish to be represented in the model, the cells are approximated as hexagons. Using hexagons enables for an elegant managing of the cells' shapes in the dish and the viral transmission. Since the culture dishes are grown to confluence, the cells are close enough that they push on each other and the cell walls deform. This causes the cells to no longer be in the shape of a circle, but become irregular polygons with multiple sides (Brückner and Janshoff 2018). Modeling the cells as hexagons gives the cells definite sides and the cells are able to span any two dimensional region forming a hexagonal grid. Furthermore, by using a hexagonal grid, when virus particles spread among this population of cells the indexing of the grid can be used to find the neighbors of any cell. This will be used for cell-free transmission to know where virus will flow away from (high concentrations areas) and to (low concentration areas) during diffusion. In addition to helping with the physical representation of the model, hexagonal coordinates have some other attributes that can be utilized to optimize the code for quicker compute times. The three attributes that this code utilizes are:

1. The coordinates can be split in to three sectors where the coordinates X_{hex}, Y_{hex}, and Z_{hex} are simply cyclic permutations.

2. The X_{hex} and Z_{hex} directions can be used as indices of a matrix.

3. The coordinates of the neighboring hexagons are found by adding a cyclic permutation of $\begin{bmatrix} 1 \\ 0 \\ -1 \end{bmatrix}$ for three of the neighbors and $\begin{bmatrix} 1 \\ -1 \\ 0 \end{bmatrix}$ for the other three neighbors.

These attributes save time by either reducing the number of calculations needed or the amount of searching through data arrays. Attribute 1 allows for only a third of the cell locations to be calculated and Attributes 2 and 3 give the data a reference so that adjacent data in memory can be found quicker.

2.1.2 Agent-based model

In an ABM, a system is broken down into smaller units called "agents". Each of the agents are governed by a set of rules on a local scale with large scale phenomena resulting from interaction of the agents, so the two scales are studied to find the connections. As a simulation of the model is stepped through time, the agents act and interact. These actions cause bulk properties, that may appear disconnected from the individual agents, to manifest. Properties are observed and measured to find the connection between the small interactions and large scale properties.

In this work, an ABM governs the transitions a cell makes through the stages of infection: healthy, eclipse, infected, and dead. A cell in the healthy state is an uninfected cell that remains healthy until infected. A cell in the eclipse state is an infected cell that is not yet producing virus. The cell remains in the eclipse state for an average amount of time, τ_E. The specific time value for each cell is determined by a gamma distribution with shape value η_E and scale value τ_E/η_E. A cell in the infected state is an infected

cell that is producing virus. The cell remains in the infected state for an average amount of time, τ_I. The specific time value for each cell is determined by a gamma distribution with shape value η_I and scale value τ_I/η_I. A gamma (Erlang) distribution is used for the amount of time in the eclipse and infected phase, as suggested by the work of Beauchemin et al. (Beauchemin et al. 2017) and Kakizoe et al. (Kakizoe et al. 2015). A cell in the dead state is a cell that can no longer change state, so once a cell is in the dead state the cell remains in that state until the end of the simulation. The flow of this is illustrated in figure 2.1.

The ABM uses four time arrays to track and transition the cells to different states after infection. The four arrays universal time (UT), healthy time (HT), eclipse time (ET), and infected time (IT) have an element for each cell. The universal time array holds the amount of time that each cell has been in the simulation; each element starts at zero and increases each iteration by the simulation's time step. The healthy time array holds the amount of time that a cell is healthy; each element starts at zero and while the cell is healthy increases each iteration by the simulation's time step. The eclipse time array holds the amount of time each cell is in the eclipse state and the infected time array holds the amount of time each cell is in the infected state. For the eclipse and infected arrays the amount of time is fixed and the value is determined by a gamma (Erlang) distribution, as described above. The flow of this is illustrated in figure 2.1.

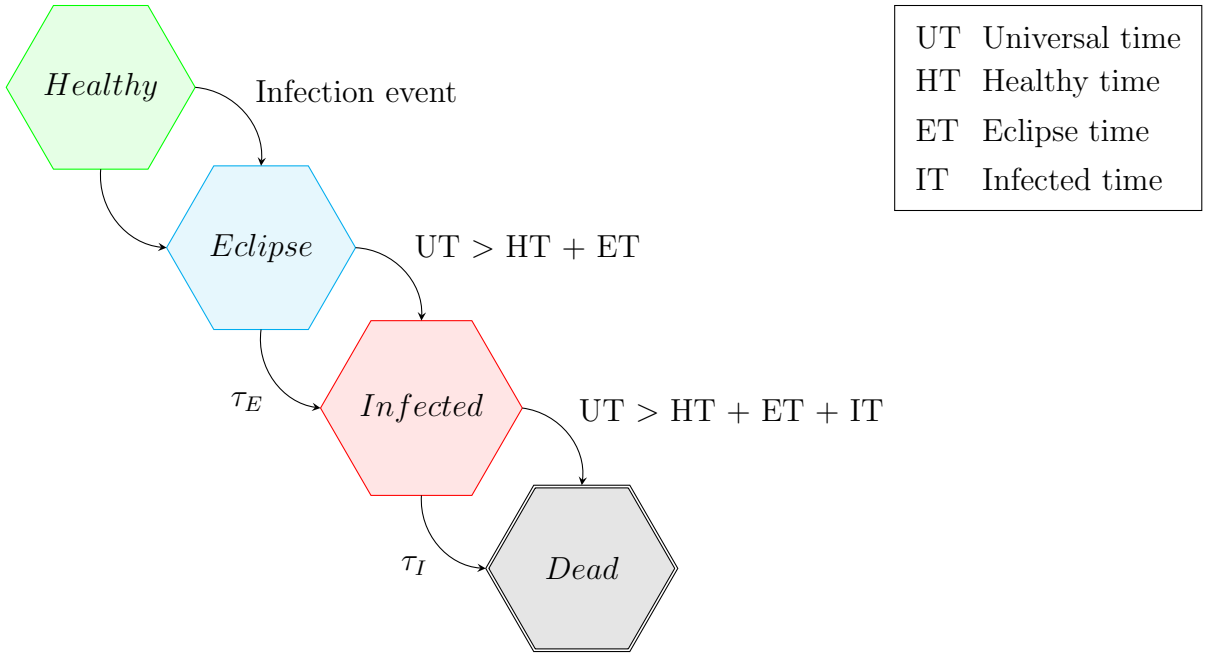

Figure 2.1: The stages of infection: healthy, eclipse, infected, and dead are shown. The cells transition through the stages at different time points. Above: The time point when a state transition occurs is shown in terms of UT, the universal time, for a cell. Below: The time point when a state transition occurs is shown in terms of average time. τ_E is the average time a cell stays in the eclipse stage and τ_I is the average time a cell stays in the infected stage. UT is the time a cell has existed, HT is the time a cell has been healthy, ET is the time a cell is in the eclipse phase, and IT is the time a cell is in the infected phase.

2.1.3 Partial differential equation model

PDMs are used to model multiple dimensions; in this work a partial differential equation in hexagonal coordinates is used to model the two-dimensional spatial spread of virus over cells in a culture dish. In a PDM, the dynamics of a system can be represented by a partial differential equation, or more specifically, an equation that contains multi-variable functions that represent important system aspects and one or more partial derivatives of those functions. In the culture dish, as an infected cell releases virus into the extracellular fluid, the virus diffuses across a density gradient. The PDM represents this diffusion with the diffusion equation,

$$\frac{\partial V}{\partial t} = D\nabla^2 V + p - cV, \tag{2.1}$$

where V is the density of the virus, D the diffusion coefficient, p is the production rate per cell, c is the viral clearance rate. In the code, along with the assumption of hexagonal cells, the cells are assumed to be flat, so the virus is diffusing over a smooth two dimensional plane. This assumption allows for the use of the two dimensional diffusion equation in hexagonal coordinates, so Eq. (2.1) becomes

$$\frac{\partial V}{\partial t} = D\frac{2}{3}\left(\frac{\partial^2}{\partial x_1^2} + \frac{\partial^2}{\partial x_2^2} + \frac{\partial^2}{\partial x_3^2}\right) V + p - cV$$

where $\mathbf{x}_1 = \begin{bmatrix} 1 \\ 0 \end{bmatrix}$, $\mathbf{x}_2 = \begin{bmatrix} -1/2 \\ \sqrt{3}/2 \end{bmatrix}$, and $\mathbf{x}_3 = \begin{bmatrix} -1/2 \\ -\sqrt{3}/2 \end{bmatrix}$ are the unit vectors for a hexagonal grid. For computation, a forward Euler implementation of the PDM with Neumann boundary conditions is used.

2.1.4 Viral transmission

When a virus is spreading among the cells in a culture dish, there is a probability that a healthy cell becomes infected by virus that is not within a cell, but flowing around and above the cell. When this viral transmission occurs it is called cell-free transmission. For cell-free transmission, the probability per unit time ($\mathrm{P_{cf}}$) that a cell becomes infected is determined by the amount of virus that is covering the cell (V) times the infection rate (β) (Holder et al. 2011a),

$$\mathrm{P_{cf}} = V\beta.$$

As a healthy cell becomes surrounded by more virus, the probability of cell-free infection increases. If the probability ($V\beta\Delta t$) is ever greater than one due to the build up of virus, an adaptive time step is used. The time step (Δt) is divided in half repeatedly until the probability of cell-free infection is below one. Once the probability is finalized, a number from the uniform distribution is compared with the probability of cell-free infection. If that number is less than $\mathrm{P_{cf}}$, then the cell becomes infected.

2.1.5 Parameters of viral spread

The eight parameters β, τ_E, η_E, τ_I, η_I, p, c, and D affect the dynamics of virus spread in the model. Four of the parameters, τ_E, η_E, τ_I, and η_I, are used in the ABM to choose the time duration that a cell is in the eclipse and infected phase as mentioned in section 2.1.2. Three of the other parameters, p, c, and D, are used in the PDM and characterize the differential equation, as mentioned in section 2.1.3. The final parameter, β, governs the interaction between the virus and cells, setting the probability that the cell is infected.

Table 2.1: Parameter values to simulate an influenza infection with the ABM/PDM model.

Parameter	Meaning	Value	Reference
β	Infection rate	2.0 /h	Scaled from Beauchemin et al. (Beauchemin et al. 2008)
p	Viral production rate	562800 /h	Scaled from Beauchemin et al. (Beauchemin et al. 2008)
c	Viral clearance rate	0.105 /h	Beauchemin et al. (Beauchemin et al. 2008)
D	Diffusion coefficient	2.16×10^{-8} m^2/h	Stokes-Einstein equation
τ_E	Mean eclipse duration	6.0 h	Beauchemin et al. (Beauchemin et al. 2008)
η_E	Eclipse shape parameter	30	Pinilla et al. (Pinilla et al. 2012)
τ_I	Mean infectious lifespan	12.0 h	Beauchemin et al. (Beauchemin et al. 2008)
η_I	Infectious shape parameter	100	Pinilla et al. (Pinilla et al. 2012)

In order to model a particular virus, values for these parameters need to be chosen. The initial values of the parameters are chosen from ordinary differential equation models of influenza and listed in Table 2.1, viral titer units have been converted to virions as described in previous work (Dobrovolny and Beauchemin 2017).

2.2 Computational details

In this work, the simulations are of viral infections, that can have drastic effects on those infected, so the model needs to produce simulations that are fast, numerically sound, and have realistic results. The model uses parallel processing on graphics processing units (GPUs) to reduce simulation times without reducing complexity. Additionally, the simulations are tested for numerical convergence and are then fit to real experimental data in order to reproduce experiments.

2.2.1 Implementation on GPUs

As the model becomes more complex, GPU acceleration via parallel programming is used to decrease the simulation run times and therefore increase the number of studies that can be conducted in a given time. In the simulations, the cells change state based on

the amount of virus above them. The number of cells in a culture dish is on the order of 10^6 cells (Thermofisher), so the ABM will simulate a grid of 1001365 agents of hexagonal cells in a circle to best replicate what is happening in the experiment. Each agent will follow the rules of checking the amount of virus above the cell every time step. Utilizing attribute 2 of hexagonal coordinates from section 2.1.1, the number of calculations is reduced from the order of ($\mathcal{O}(n^2)$) per time step to the order of the number of agents ($\mathcal{O}(n)$). The calculations from the agents' rules are split over the processing units of a GPU to be calculated in parallel or simultaneously. To utilize this processing, Nvidia's CUDA (Compute Unified Device Architecture) is used to implement the ABM and PDM. CUDA is an Application Programming Interface (API) that allows the many processing units (cores) on a Nvidia brand GPU to be used for computing.

2.2.2 Convergence Testing

Partial differential equations (PDEs) are a popular way to model systems that evolve over both space and time, but often require computers to produce solutions. With PDEs, even systems that have an exact solution often need to be calculated on a computer because of the infinite series that are required in those solutions. Therefore, solutions to PDEs are often found through numerical integration. In the numerical integration, space and time are assumed to be made up of small units or discretized. From this discretization, time is a one dimensional line of points separated by a chunk of time called Δt and two dimensional Cartesian space is a grid with a line of points for each dimension where there is a chunk of space for each dimension Δx, Δy. At these points in time and

space, a numerical integration scheme approximates the solution of the PDE. Different numerical schemes have different benefits. Depending on the phenomena that needs to be studied with the PDE the size of Δt, Δx, and Δy and the choice of numerical scheme are important. If the chunks of space or time are too large then the simulation does not have the resolution to resolve phenomena that occur at smaller increments in the model and if the numerical scheme requires to much computing power then the solutions can not be found in a timely manner.

Depending on the choice of numerical scheme, a conditional relationship between Δt, Δx, and Δy must be met. For the symmetric, two dimensional Euler's method

$$\Delta t \leq \frac{(\Delta x)^2}{4D},$$

is the conditional relationship (Wendroff 1968, Olsen-Kettle). Satisfying this relationship is necessary to ensure that the sequence of approximations that the numerical scheme uses to approximate a solution converges, otherwise the error grows exponentially to a point that the solutions are unreliable. Using the relationship above, values for Δt, Δx, and Δy can be chosen to ensure stability of the error in the numerical scheme. As long as that relationship is met the solution is reliable within a certain error, but the relationship does not give the Δt, Δx, and Δy that are best for producing accurate simulations with the least amount of computing cost.

To ensure the simulations are not using more resources than necessary, the space and time discretizations: Δt, Δx, and Δy need to be optimized. Convergence testing is a simple brute force method where the input parameters are increased or decreased

by a particular amount and the accuracy or trends of the simulation are measured for each of the the new increments. Schemes for convergence testing are implemented and studied in fields like computational fluid dynamics (Bermejo and Saavedra 2016, Kim and Kim 2020) and astrophysics (Xu and An 2021, Banei and Shanazari 2021). The model proposed in this work has fixed Δx and Δy to a value of 50 µm, because the simulations are of real cells, whose average diameter can be measured between 50–100 µm. Thus the convergence testing only has to be conducted for Δt. To conduct the study a starting point of 0.005 hr, about 5.78 times smaller than the conditional relationship, was chosen and a range of seven values was created by multiplying or dividing the initial Δt by 2 repeatedly. For each of these Δts, the median viral titer curve of ten simulations were compared.

2.2.3 Measurements

As the viral infection progresses the total amount of virus in the culture dish changes and the shape of the total amount of virus over time can change depending on the virus being used for the infection. Plotting the amount of virus vs. time produces a curve that has a distinct shape and has characteristics that can be measured. The measurements, shown in Figure 2.2 and defined below, can be used to compare multiple viruses or to compare multiple simulations of the same virus with different input parameters. In this thesis, I will use them to verify the convergence of the simulation.

- **peak viral load:** The maximum amount of virus is commonly used as an indicator of the transmissibility of an infection (Handel et al. 2009).

- **time of viral peak:** This is the time between the start of the infection and the peak of the virus and can give an indication of how quickly the virus is replicating.

- **viral upslope:** Viral upslope is the exponential growth rate of the viral titer before the peak is reached and is another indication of how quickly the virus is spreading from cell to cell.

- **viral downslope:** Viral downslope is the exponential decay rate of the viral titer after the peak. While the slope during the decay phase is negative, we define downslope as the positive value of the slope.

- **area under the curve (AUC):** AUC is often used to assess the severity of an infection (Hayden et al. 2000, Barroso et al. 2005).

- **infection duration:** The infection duration is indicative of how long an infected patient might test positive for presence of the virus. In this work 10^1 virions is the threshold.

2.3 Data Fitting

As part of the model validation, the model is tested to ensure it can reproduce viral titer curves observed experimentally. Three experimental data sets varying both virus and cell type are being used. The first data set used here is from an *in vitro* experiment performed by Pinilla et al. (Pinilla et al. 2012). During the study, a well of a 24-well plate, containing Madin-Darby canine kidney (MDCKα2,6) cells was inoculated with the

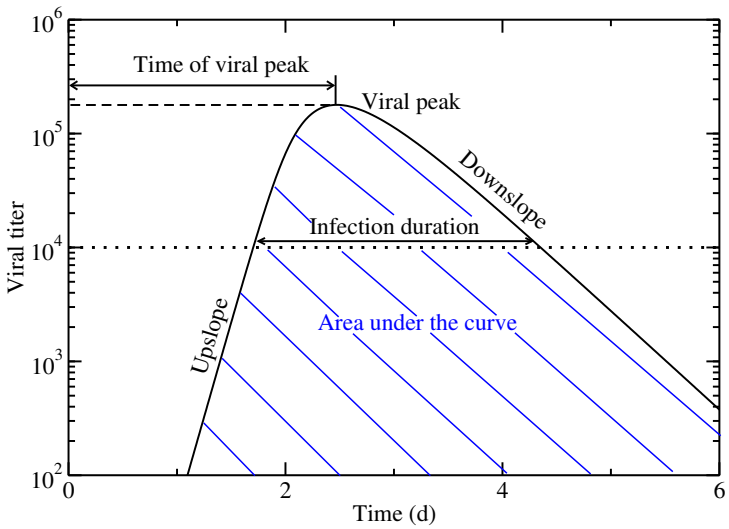

Figure 2.2: Measurable characteristics of the viral titer curve.

A/Québec/144147/09 (H1N1) pandemic strain of influenza virus and the supernatant fluid was collected every 6 hours until 36 hours and then every 12 hours until 72 hours post infection. The supernatant was then used for ribonucleic acid (RNA) isolation and/or viral titration by standard plaque assay on MDCKα2,6 cells. The specific data referenced for this work is the "Multiple-cycle viral yield" experiment shown in figure 2A of the Pinilla et al. manuscript.

The second and third data sets are from an *in vitro* experiment performed by Wang et al. (2021). During the study, 25 cell lines were inoculated with 5×10^4 $TCID_{50}$ (50% Tissue Culture Infectious Dose) per well of SARS-CoV-2/USA-WA1/2020. The Vero and Vero76 cell line data will be used here for the fitting process. The supernatant fluid was recorded initially at 0 hours and washed away at 2 hours. Supernatent was then collected every 24 hours until 120 hours post infection. The supernatant was used for viral RNA quantification. The specific data referenced for this work is the Vero cell lines and the Vero76 cell lines of the "Replication of SARS-CoV-2 in a Large Set of Cell Substrates"

experiment shown in figure 2 of the Wang et al. manuscript. Data was extracted from both manuscripts using WebPlotDigitizer (WebPlotDigitizer).

To determine the best fit of the model to the experimental data, the sum of square residuals (SSR) is minimized,

$$\text{SSR} = \sum_{i=1}^{n} (y_i - \hat{y}_i)^2,$$

where y_i is from the experimental data set and $\hat{y}_i$ is from the simulated data set. In our case, the simulated data set is the average of ten cell-free transmission simulations. The initial conditions for the simulations are: Total cells – 1001365, Total virus – 0.0, and Multiplicity of Infection (MOI) – 5×10^{-5}. To perform the minimization, a separate code that utilizes the function `minimize` from the python package `scipy`, was written. In the code, five parameters (β, p, τ_I, τ_E, and c) are allowed to vary and the remaining parameters are held fixed to the values given in Table 2.1. The minimization code is given an initial guess for the five parameters, then by the Nelder-Mead method the next set of parameters is produced, until the minimum SSR is found.

2.4 Summary

In this chapter, I've described the construction of a hybrid ABM/PDM model of viral infections and I've outlined the techniques that will be used to test the reliability and validity of the model.

Chapter 3

Results

The methods presented in the previous chapter result in a model for studying viruses that incorporates the spatial spread of virus, has the ability to produce simulations in seconds, and has the flexibility to be applied to real data. In this chapter, the accuracy, speed, and applicability of the model is presented. I will show accurate simulations of plaque assays, the speed increase of the simulations by GPUs, and the analysis of virus infections.

3.1 Model simulation

Using the influenza parameters of table 2.1, I simulated infections initiated with 1001365 cells in a dish, of which 100 randomly chosen cells are infected and no initial virus. Figure 3.1 shows different views of plaques forming in the entire dish. On the left are cells in the different stages of infection described in section 2.1.2, where the healthy cells are colored green, eclipse cells are colored cyan, infected cells are colored red, and

dead cells are colored black. On the right are figures showing the corresponding virus concentrations that are over the cells, where areas of higher concentration are colored yellow and areas of lower concentration are colored purple. Figure 3.1 shows the infection in 5 hour increments starting at 5 hours, when no cells are producing virus, and ending at 60 hours, when almost all the cells have died. The ABM reproduces the plaques typically seen in experimental *in vitro* infections (Holder et al. 2011b).

For a closer look at the plaques, figure 3.2 is a zoomed in view of the infection at hours 6.5, 11.5, and 16.5. The cells are shown on the left, with the same color scheme used in figure 3.1, and the corresponding virus distribution is shown on the right. Here the heterogeneous growth of the plaque can clearly be see; it is not simply a radially symmetric change of cells from eclipse to infectious.

As a visual check, the simulated plaque assays are compared to actual plaque assays. The left of figure 3.3 is a petri dish from a plaque assay that infected MDCK cells with influenza virus A/Memphis/14/96-M (H1N1). The virus was placed in the dish and then after one hour a solution of Avicel RC-581 was injected onto the cells. The Avicel RC-581 allows for plaques to form by hindering the flow of virus through the liquid medium in the dish. When the experiment was done, the assays were stained with an immuno-stain that stains the infected cells red. The right of figure 3.3 shows the simulated assay of 10^6 cells, where again the same color scheme as figure 3.1 is used; the healthy cells are colored green, eclipse cells are colored cyan, infected cells are colored red, and dead cells are colored black. The plaques appear to be similar between the actual and simulated assays.

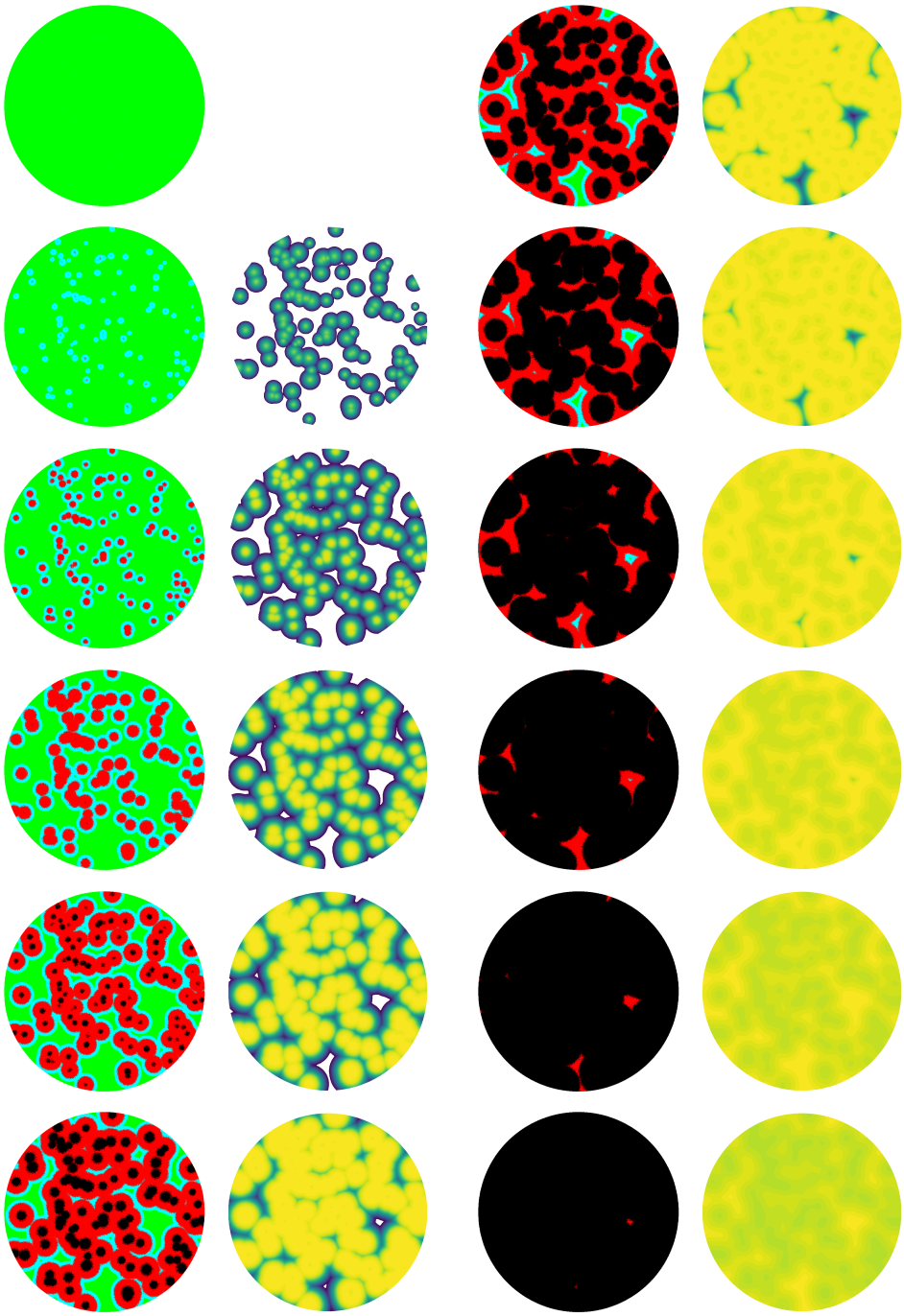

Figure 3.1: The dish at hours 5 through 60 in 5 hour increments. On the left are cells in the different stages of infection; the stages are represented by healthy cells colored green, eclipse cells colored cyan, infected cells colored red, and dead cells colored black. On the right are images of the virions that are diffusing over the cells; areas of higher concentration are represented by yellow and areas of lower concentration are represented by purple.

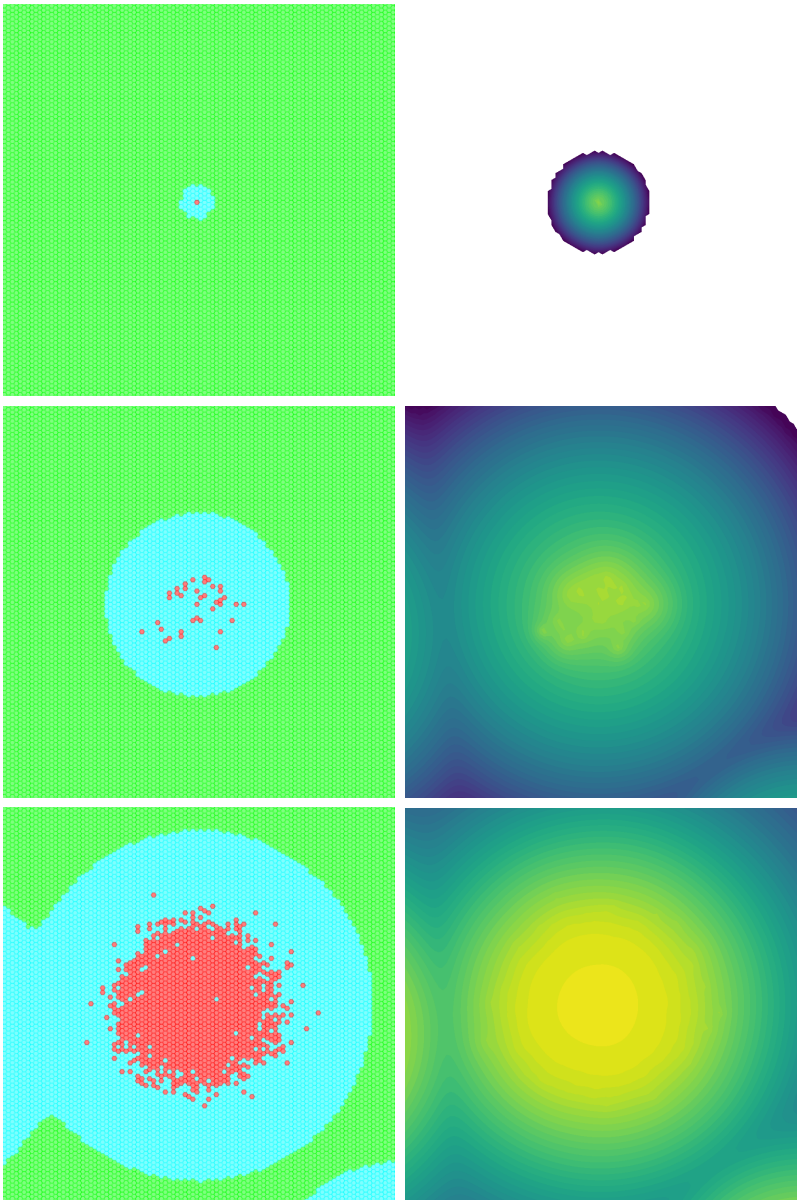

Figure 3.2: A zoomed in section of the dish looking at the plaque formed by a single infected cell during a viral infection at hours 6.5, 11.5, and 16.5. On the left are cells in the different stages of infection; the stages are represented by healthy cells colored green, eclipse cells colored cyan, infected cells colored red, and dead cells colored black. On the right are the many virus that are diffusing over the cells; areas of higher concentration are represented by yellow and areas of lower concentration are represented by purple.

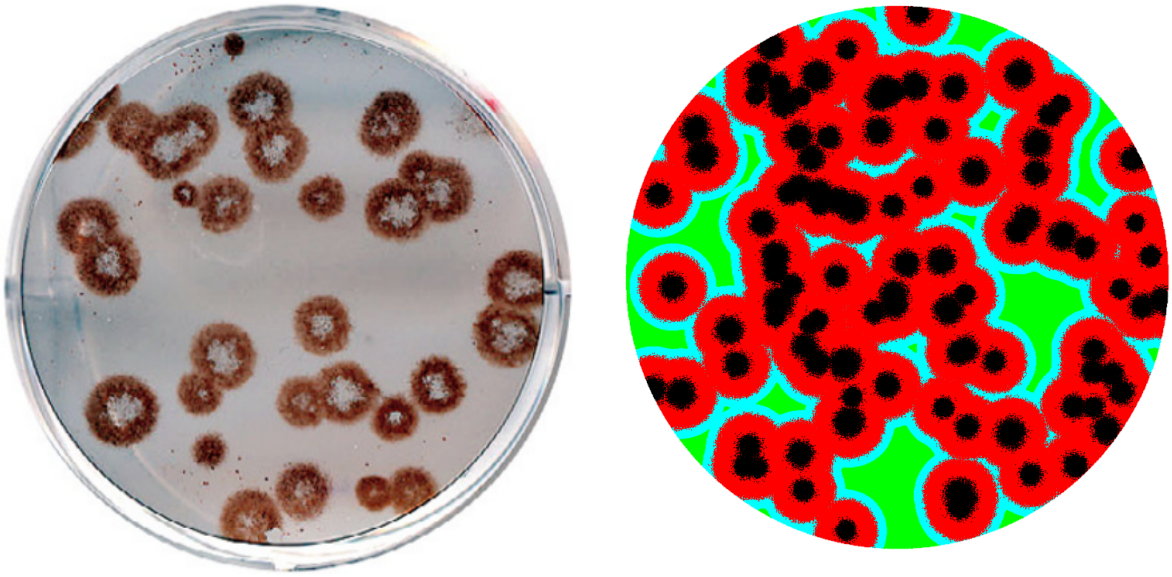

Figure 3.3: (Left) Plaque assay that infected MDCK cells with influenza virus A/Memphis/14/96-M (H1N1). (Right) Simulated plaque assay of 10^6 cells, where the green are the healthy cells, cyan are the eclipse cells, red are the infected cells, and black are the dead cells.

3.2 Implementation on GPUs

Ten viral infections of five different numbers of cells were simulated, with codes that utilize three different programming languages: Python, C, and CUDA. The amount of computation time needed to simulate one hour of the infection, on a desktop computer, is shown in figure 3.4. The computer was built with an Intel Xeon E-2144G central processing unit (CPU), 16 gigabytes of random access memory (RAM), and P4000 Nvidia Graphics card. The compute times for the three codes increase as the number of cells in the simulations increases, but the speed increase of switching from Python, the programming language commonly used in physics, to code using CUDA for implementation on GPUs is 7000 times faster.

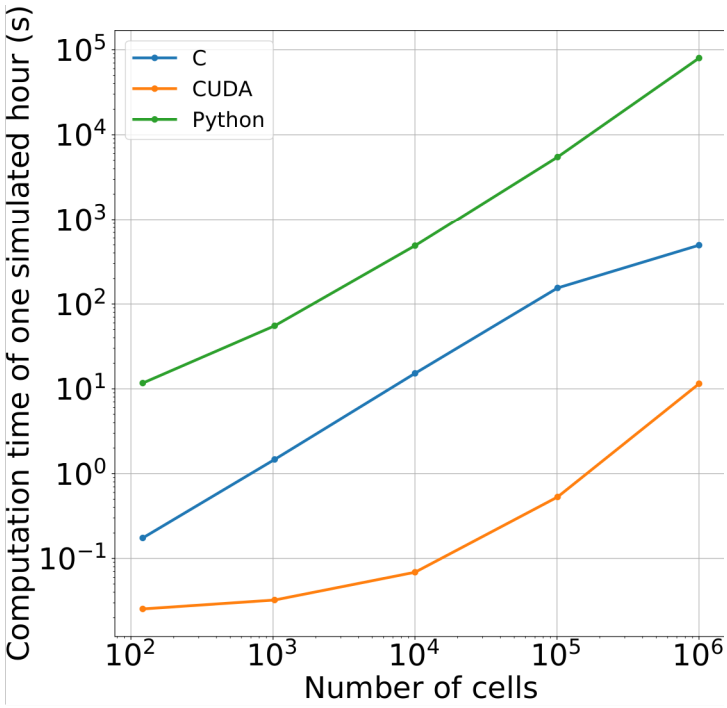

Figure 3.4: With more than a million cells, CUDA is 7000 times faster then the Python code and 43 time faster than the C code.

3.3 Convergence Testing

Three scenarios were examined when testing the convergence of the model: an infection initiated with 10013 cells in the eclipse phase (Initial Cell); an infection initiated with 10^{12} virions (Initial Virus); and a scenario with no infection, but 10^{12} virions (Only Virus), examining viral spread and decay only. Simulations in each of the scenarios used the influenza parameters from table 2.1. Figure 3.5 shows the simulations of the three scenarios, where the time step was varied to test the convergence of the model in time. A time step of 0.005 hr, about 5.78 times smaller than the conditional relationship from section 2.2.2, was chosen and a range around it was made by dividing or multiplying by 2 repeatedly. This formed an array of seven time step values, 0.000625, 0.00128, 0.0025, 0.005, 0.01, 0.02, and 0.04 hr. For each time step, the median curve of ten viral titer

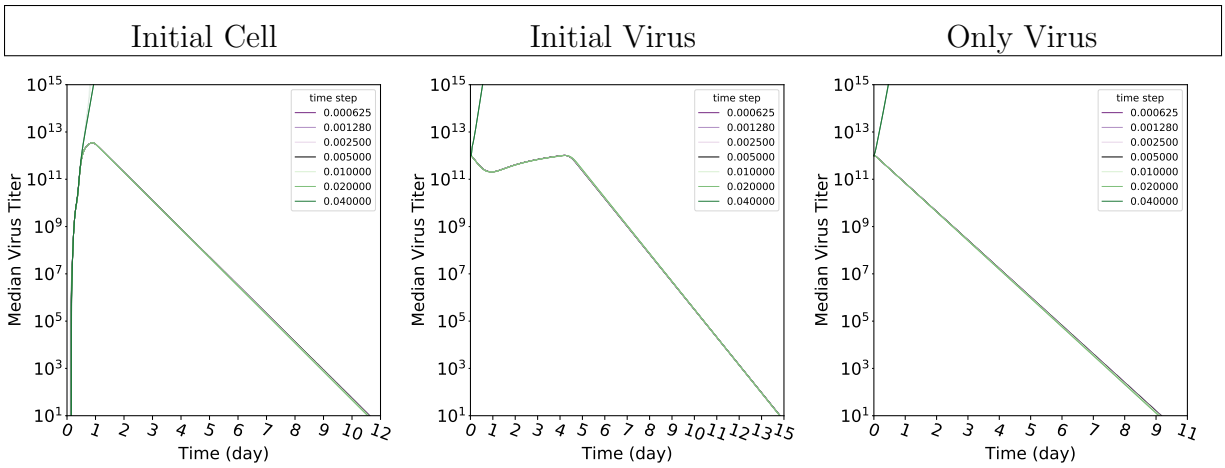

Figure 3.5: The time step was varied to test the convergence of the model in time. A time step of 0.005 hr was chosen and a range around it was made by dividing or multiplying by 2 repeatedly. Seven values were used [0.000625, 0.00128, 0.0025, 0.005, 0.01, 0.02, 0.04]. The median curve of ten viral titer curves is shown for each time step. From left to right, curves of a viral infection exhibiting cell-free transmission initiated with infected cells; curves of a viral infection exhibiting cell-free transmission initiated with virus; and curves of virus without underlying cell infection.

curves is shown. In figure 3.5, from left to right, curves of a viral infection initiated with infected cells; curves of a viral infection initiated with virus; and curves of virus without underlying cell infection. For all time steps, except 0.04 hr, the curves are hard to distinguish from one another and follow the same trend for each scenario.

In figure 3.6 the different viral titer curves are explored further by plotting the measurable characteristics mentioned in section 2.2.3 for each time step. For all the characteristics, except AUC, the amount of change was in the hundredths place or less, so for time characteristics the amount of change was less than 14.5 min, for 1/time characteristics the amount of change was less than $6.9 \times 10^{-6}\,\mathrm{min}^{-1}$, and for amount of virus characteristics the amount of change was less than 10^{10} virus particles, which is less than 1 % change in the amount of virus. Note that typical experimental error in measurements of viral load are typically 0.5 $\log_{10}$(PFU/ml) (LaBarre and Lowy 2001). The AUC varied the most

over the different timesteps. The mean of the AUC values for the different timesteps is 3626 log(virus)/d with a standard deviation (STD) of 13.09 log(virus)/d. Therefore, the coefficient of variation is $CV = \frac{13.09}{3626} \approx 0.0036$, which shows that the STD is about 0.36 % the size of the mean.

3.4 Fitting the model to data

The model is fit to three experimental *in vitro* data sets (Pinilla et al. 2012) and (Wang et al. 2021) via minimization of the SSR. For the (Pinilla et al. 2012) data, the initial condition of the simulations were: 501535 cells in the dish (similar to the number of cells in a typical 24-well plate (Thermofisher)), 250 initial infected cells, and no virus in the dish. On the left in figure 3.7 is the median curve of ten simulations, using the best fit parameters, plotted in dark blue alongside the data in green. For both of the cell lines used from the (Wang et al. 2021) data, the initial condition of the simulations were: 501535 cells in the dish (similar to the number of cells in a typical 24-well plate), 0 initial infected cells, and 5×10^4 virus in the dish. In the center and on the right of figure 3.7 are the median curves of ten simulations, using the best fit parameters, plotted in dark blue alongside the data in green. The best fit parameters for each set of data are presented in table 3.1.

From the best fit parameters in table 3.1, 100 simulations for each data set were produced. All one hundred runs and the median curve for each data set are shown in figure 3.8. To showcase how the different parameters change the viral titer, the initial conditions of the simulated dish were the same for the different data sets. The initial

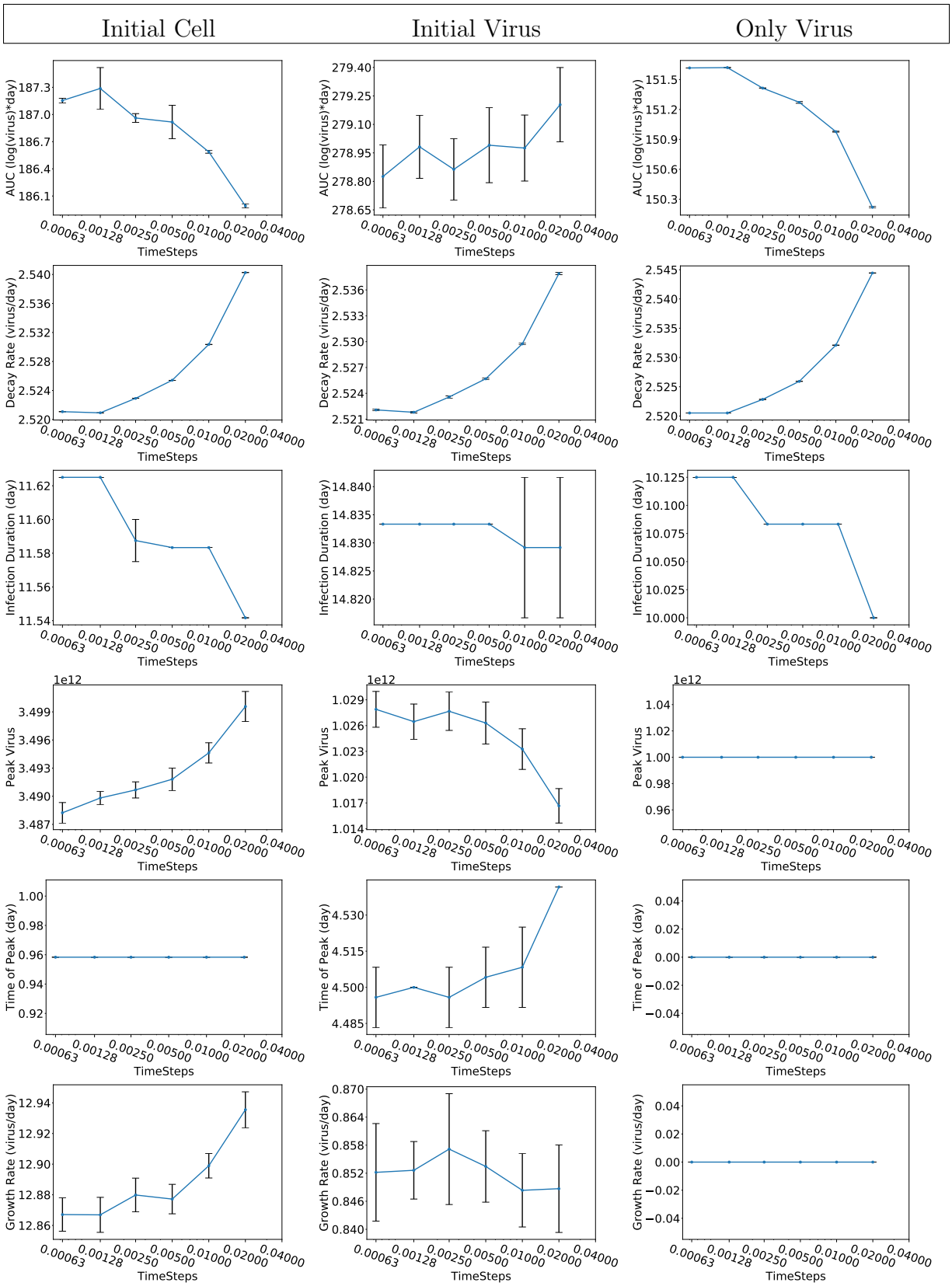

Figure 3.6: Characteristics of the viral titer curves where measured for each of the seven time steps and the different scenarios.

Table 3.1: Best fit parameter values from fitting the model to experimental data (Pinilla et al. 2012, Wang et al. 2021).

Parameter	Meaning	Pinilla et al. Value	Wang et al. Vero76 Value	Wang et al. Vero Value
β	Infection rate	$54\,\mathrm{h}^{-1}$	$56\,\mathrm{h}^{-1}$	$69\,\mathrm{h}^{-1}$
p	Viral production rate	$3000\,\mathrm{h}^{-1}$	$3.9\,\mathrm{h}^{-1}$	$2.4\,\mathrm{h}^{-1}$
c	Viral clearance rate	$0.25\,\mathrm{h}^{-1}$	$0.01\,\mathrm{h}^{-1}$	$0.06\,\mathrm{h}^{-1}$
D	Diffusion coefficient	$2.2 \times 10^{-8}\,\mathrm{m}^2\,\mathrm{h}^{-1}$ (fixed)	$1.7 \times 10^{-8}\,\mathrm{m}^2\,\mathrm{h}^{-1}$ (fixed)	$1.7 \times 10^{-8}\,\mathrm{m}^2\,\mathrm{h}^{-1}$ (fixed)
τ_E	Mean eclipse duration	16 h	2.9 h	3.8 h
η_E	Eclipse shape parameter	30 (fixed)	30 (fixed)	30 (fixed)
τ_I	Mean infectious lifespan	26 h	17 h	18 h
η_I	Infectious shape parameter	100 (fixed)	100 (fixed)	100 (fixed)

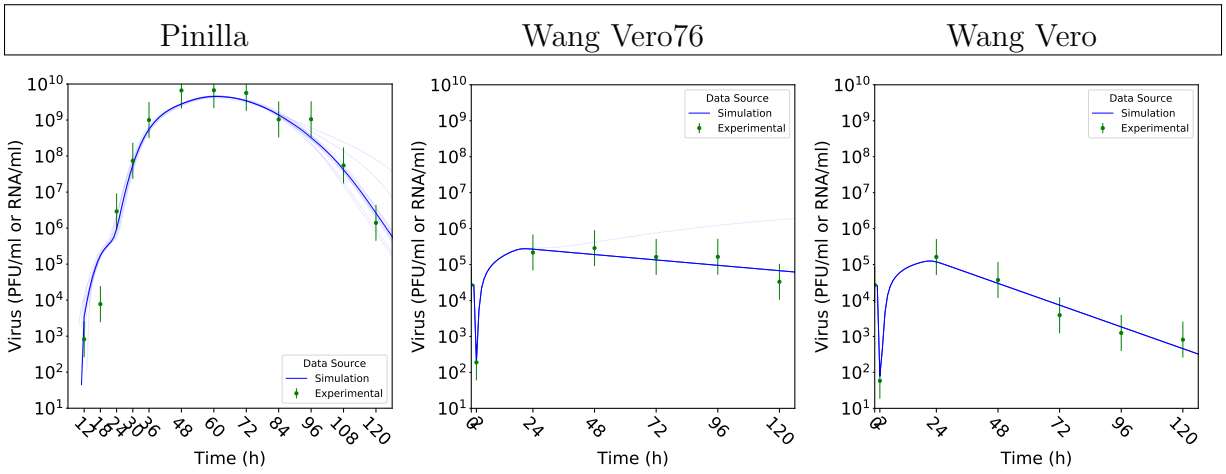

Figure 3.7: The ten simulated titer curves and corresponding median curve, from the fitting process, are plotted in blue. The experimental cell-free transmission data (Pinilla et al. 2012) is plotted in green. The median curve has the minimal SSR with respect to the experimental data, when using the best fit parameters. The best fit parameters are shown in 3.1.

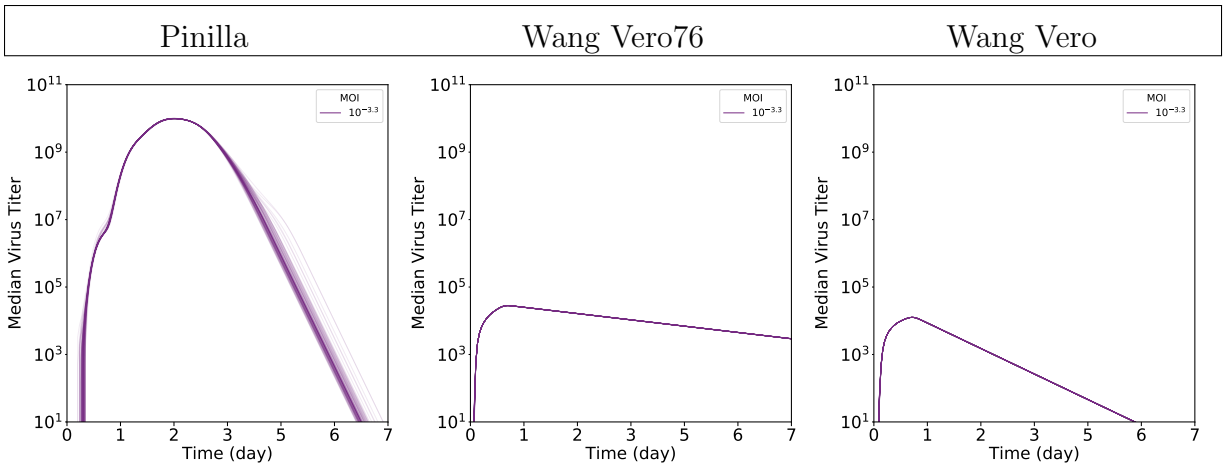

Figure 3.8: Using the best fit parameters in table 3.1, a hundred simulated titer curves and corresponding median curve are plotted in purple.

conditions were: 1001365 cells in the dish (similar to the number of cells in a typical 35 mm petri dish), 500 initial infected cells, and no initial virus in the dish. It is easy to notice in figure 3.8 that the simulations of the Pinilla et al. data vary more than simulations of the Wang et al. data; this is from the change in standard deviation of the eclipse phase length of the cells. This will be discussed more in section 4.1 of the discussion chapter.

3.5 Summary

In this chapter, I've shown that the model produces accurate simulations that compare to real experimental plaque assays and that the model can reproduce experimental data.

Chapter 4

Discussion

In the previous chapter it was shown that the model is accurate, fast, and numerically sound. Then it was shown that the model can reproduce experimental influenza virus and SARS-CoV-2 experiments from real data. In this chapter, the findings, model extensions, and future work of this thesis will be discussed. I will discuss how the faster speed of the simulations allows for the model to be compared with common practices in the field of computation virology, how the current limitation of a lack of all the cell processes can be addressed, and how the model will be applied in the future.

4.1 Findings

4.1.1 Advances in ABM simulation

In this paper, the construction of a hybrid ABM/PDM model to investigate spatially extended viral infections is described. While the formulation of the model is similar to other ABM/PDM models of viral spread (Beauchemin et al. 2005, Bauer et al. 2009),

the model was implemented to run on GPUs, vastly improving the simulation speed of these models. This allows for efficient replication of *in vitro* infections with a realistic number of cells. This will help lead to a better understanding of virus-cell dynamics *in vitro* (Blahut et al. 2021), but could also help realize the goal of simulating infections *in vivo* (Laubenbacher et al. 2021). The faster simulations also allowed for the use of standard ordinary differential equation (ODE) model-fitting techniques to fit this model to experimental data, making it possible to quickly parameterize these models to reproduce dynamics of different viruses. Previously, researchers have had to develop other techniques to help speed up fitting of ABMs to experimental data, including reducing the sampled parameter space (Li et al. 2017), and mapping of ABM outputs to simpler functions (Tong et al. 2015, Read et al. 2016). These techniques coupled with simulation of ABMs on GPUs could potentially allow for real-time parameter estimation of models for use in patient care. This is particularly useful for a novel pandemic virus that can be simulated such that trial runs of test drugs can be performed and viral infection severity for a patient can potentially be predicted.

This paper shows that the use of GPUs to accelerate computation of agent-based and partial-differential equation hybrid models allows for simulation results within hours, but with the necessary level of detail to capture individual cell effects, and allows for parameterizing the model quickly. The model in this work accurately replicates the diffusion of a virus, the stages of infection of individual cells, and can be fit to data within hours. While still lacking some of the biology needed for replication of *in vivo* infections, the speed of computation leaves room for incorporation of additional features. Thus, this model implementation forms the foundation of a modeling and simulation

tool that can accurately predict in-host viral dynamics and be quickly deployed to help combat the next pandemic.

4.1.2 ABM viral dynamics

From the data fitting results shown in section 3.4, some of our parameter estimates differ from those reported in Pinilla et al. (Pinilla et al. 2012) even though the same data was used. Our best fit τ_I is smaller than the $\tau_I = 49\,\mathrm{h}$ reported by Pinilla et al., while our best fit τ_E is larger than the $\tau_E = 6.6\,\mathrm{h}$ found by Pinilla et al., and the best fit c is larger than $c = 0.13\,\mathrm{h}^{-1}$. Some of this discrepancy might be due to the inclusion of spatial effects in the ABM, but Pinilla et al. also used more data — they used both a single cycle and multiple cycle experiment as well as viral RNA measurements — to constrain the parameter estimates. All in all, the ABM/PDM model can replicate the viral titer measurements of a typical infection (both influenza virus and SARS-CoV-2) via fitting where the fitting process uses standard packaged fitting algorithms and the computational time for fitting is less than 24 hours from initial guess to best fit.

In figure 3.8, one might notice that the simulated experiments of the Pinilla et al. data vary from each other more than each simulation of the Wang et al. data. This is due to the fact that the standard deviation of the Erlang distribution that determines the eclipse phase lengths is dependent on τ_E. The mean of the phase time for the eclipse phase is τ_E and the standard deviation is $\tau_E/\sqrt{\eta_E}$. Therefore, the standard deviation becomes smaller as τ_E becomes smaller. This point is illustrated in figure 4.1, where, on the left, the Erlang distributions of the eclipse phase lengths and, on the right, the

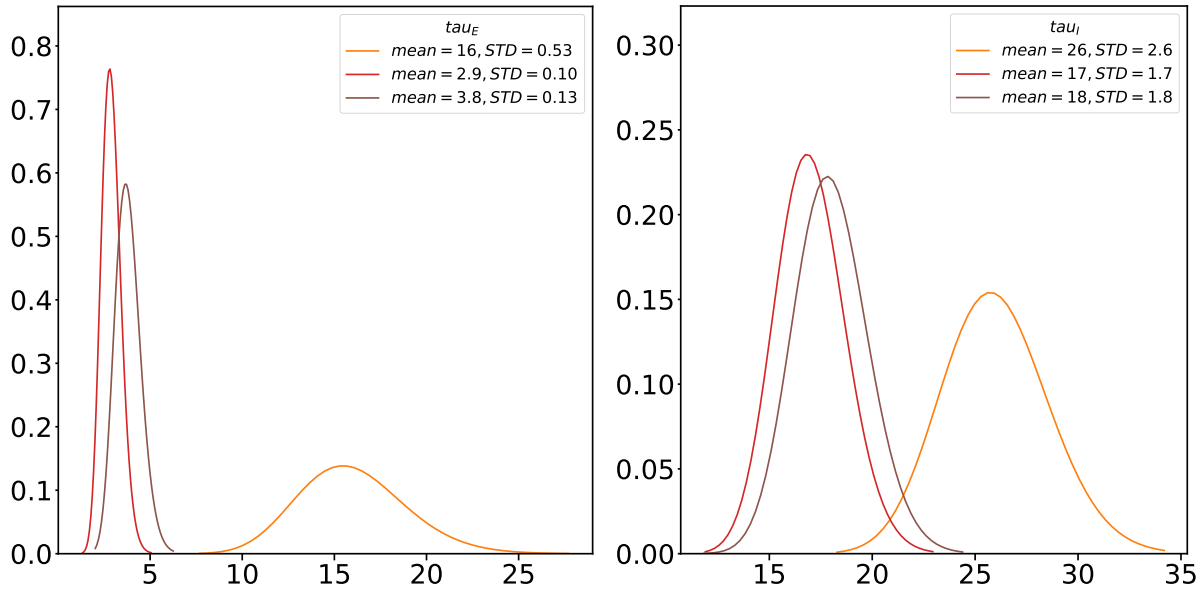

Figure 4.1: On the left is the Erlang distributions of the eclipse phase lengths and on the right is the Erlang distributions of the infectious phase lengths. For the eclipse phase and the infectious phase: MEAN $= \tau$ and STD $= \tau/\sqrt{\eta}$.

Erlang distributions of the infectious phase lengths are plotter for each of the three infections. This implies that, for cell free transmission of a virus with a small mean eclipse phase length, the variation in end times of infections for the same virus comes from the differences in infectious phase lengths.

4.2 Model extensions

Although the model currently only incorporates cell-free transmission, since the ABM models interactions of each cell in a culture dish, the spatial aspects of different viral transmission routes can be explored in detail. There has been recent interest in viruses that transmit via cell to cell transmission, with ODE (Allen and Schwartz 2015, Komarova and Wodarz 2013, Iwami et al. 2015), stochastic (Graw et al. 2015), and ABM (Kumberger et al. 2018, Blahut et al. 2021) models developed to study how cell to cell

transmission alters infection dynamics. There are also viruses that cause cells that form syncytia, which are cells that have fused into a single multi-nucleated cell. Not much is known about how syncytia alter infection dynamics, with a recent ODE model attempting to assess the effect of syncytia on viral time course (Jessie and Dobrovolny 2021), but spatial effects really need to be included for a proper assessment of the role of syncytia. Finally, advection can be added to the diffusion of the virus particles to more closely mimic the respiratory tract. Recent PDE (Quirouette et al. 2020) and ODE (González-Parra and Dobrovolny 2019) models both indicate that the addition of advection can limit the spread of respiratory viruses towards the lower respiratory tract, but the stochasticity included in an ABM might affect this result.

While the model is able to replicate a typical viral time course during an infection, it is missing many components that play important roles in the infection. For example, the immune response of the host has not been added to the model. The immune response is a large, if not the main, contributing factor to symptoms experienced during a viral infection (Manchanda et al. 2014, Zheng and Perlman 2018), but also limits spread of infection itself (Dobrovolny et al. 2013). ABMs are already used to model various aspects of the immune response (Whitman et al. 2020, Kerepesi et al. 2019, Levin et al. 2016), so the immune response can be incorporated into the existing ABM/PDM framework. Cell tropism, the preference of virus for one cell type over another, is another feature of viral infections that can be incorporated into the ABM. ODE modeling indicates that cell tropism can lead to longer lasting infections (Dobrovolny et al. 2010), but will also likely affect the spatial dynamics of infection. Finally, variation in production of virus by individual cells (Timm and Yin 2012) can be incorporated to determine how this type of

cell heterogeneity affects spatiotemporal infection dynamics.

4.3 Future Work

A goal of this research is to not only be able to predict viral infection, but it is to find ways to uncover potential causes of disease severity. The novel coronavirus, SARS-CoV-2, originated in Wuhan, China in late 2019 and rapidly spread around the world (Chen et al. 2020, Wu et al. 2020). This virus causes the Covid-19 disease, which can lead to severe illness needing long hospitalization (Sun et al. 2020, Goyal et al. 2020, Jiang et al. 2020), but at the same time a significant fraction of those who contract the virus experience an asymptomatic Covid-19 disease (He et al. 2020). It is still not entirely clear who is at risk for developing severe disease, although correlations of disease severity with levels of vitamin D (Ilie et al. 2020), levels of various immune components (Liu et al. 2020b;a, Zhang et al. 2020, Yang et al. 2020), and age (Borghesi et al. 2020, Zhang et al. 2020) have been noted. There has also been investigation of the possibility of disease severity being linked to initial viral inoculum (Little et al. 2020, Guallar et al. 2020, Gandhi et al. 2020).

The difference in viral inoculum between patients could be caused by varying amounts of virus in airborne droplets. The major route of transmission for SARS-CoV-2 is by airborne droplets (Morawska and Cao 2020). One study indicates that sneezing and coughing creates a turbulent gas cloud that can cause viral-laden droplets to spread up to 27 feet (7–8m) (Bourouiba 2020), and allows the virus to get into the ventilation system of a building. A review of literature on droplet and airborne viral spread concludes that 8

of 10 studies showed that droplets spread further than the 6 foot (Bahl et al. 2020) social distancing recommendation. While personal protective equipment is helpful in reducing the ability of virus to enter the respiratory tract, it is not perfect (Mittal et al. 2020). All of these factors lead to exposures to vastly different quantities of virus when people are going about their daily activities. Thus it is important to understand whether different initial inocula lead to different viral dynamics in patients.

There is some evidence from other respiratory viruses that the size of the initial inoculum could play a role in the severity of the illness. An influenza epidemiological modeling study suggests that a higher initial dose can lead to a higher mortality rate (Paulo et al. 2010). This is corroborated by an influenza in-host modeling study that also finds a correlation between the initial viral dose and survival rate (Price et al. 2015). Other modeling studies have found dependence of other measures of infection severity on initial dose for influenza (Moore et al. 2020), respiratory syncytial virus (Wethington et al. 2019), adenovirus (Li and Handel 2014), and porcine reproductive and respiratory virus (Go et al. 2019). There are also experimental studies that find a link between dose and infection severity. Experiments using influenza have found inoculum dose dependence of total number of infected cells and area under the curve (Manicassamy et al. 2010), peak viral titer (Ginsberg and Horsfall 1952, Iida and Bang 1963, Ottolini et al. 2005), viral growth rate (Ginsberg and Horsfall 1952), and time of viral peak (Iida and Bang 1963, Ginsberg and Horsfall 1952). Experiments with other viruses, such as adenovirus (Prince et al. 1993), and parainfluenza (Ottolini et al. 1996), have also shown correlations between initial inoculum and various measures of disease severity. If SARS-CoV-2 shows a similar pattern, initial inoculum should be considered as a possible contributor to

infection severity and adverse outcomes. With this model different scenarios can be tested to help narrow down and rule out causes a different viral infection severities.

4.4 Conclusion

In this thesis, I've presented the testing, validation, and application of a GPU accelerated, hybrid, agent-based and partial differential equation model. I demonstrated that the model incorporates the spatial spread of viruses and produces accurate simulations in a few seconds or minutes, by utilizing parallel processing on GPUs. From the speed increase, standard model-fitting techniques, such as "Minimizing the SSR", can be used to fit the model to experimental data. Now viruses can be studied in a more accurate way and parameterized in hours. By creating this model, the foundation of a modeling and simulation tool has been developed to study viruses. This work will be deployed to study different aspects of a virus, how different viruses affect infection, and what may lead to different severities of infections. Now that I've created a new in-host viral model, when the next flu season, epidemic, or pandemic comes; there will be one more tool that can help to gain insight and hopefully help end or slow the spread of the virus.

Bibliography

L. J. Allen and E. J. Schwartz. Free-virus and cell-to-cell transmission in models of equine infectious anemia virus infection. *Math. Biosci.*, 270:237–248, December 2015. doi: 10.1016/j.mbs.2015.04.001.

A. Alvarado, R. Corrales, M. J. Leal, A. De la Ossa, R. Mora, M. Arroyo, A. Gomez, A. Calderon, and J. L. Arias-Arias. Cellular-Level Characterization of Dengue and Zika Virus Infection Using Multiagent Simulation. In *2018 IEEE International Work Conference on Bioinspired Intelligence (IWOBI)*, pages 1–6, San Carlos, July 2018. IEEE. ISBN 978-1-5386-7506-9. doi: 10.1109/IWOBI.2018.8464219. URL `https://ieeexplore.ieee.org/document/8464219/`.

P. Bahl, C. Doolan, C. de Silva, A. A. Chughtai, L. Bourouiba, and C. R. MacIntyre. Airborne or droplet precautions for health workers treating coronavirus disease 2019? *J. Infect. Dis.*, 189, April 16 2020. doi: 10.1093/infdis/jiaa189.

S. Banei and K. Shanazari. On the convergence analysis and stability of the RBF-adaptive method for the forward-backward heat problem in 2D. *Appl. Num. Meth.*, 159:297–310, January 2021. doi: 10.1016/j.apnum.2020.08.015.

L. Barroso, J. Treanor, L. Gubareva, and F. G. Hayden. Efficacy and tolerability of the oral neuraminidase inhibitor peramivir in experimental human influenza: randomized, controlled trials for prophylaxis and treatment. *Antivir. Ther.*, 10:901–910, 2005.

A. L. Bauer, C. A. Beauchemin, and A. S. Perelson. Agent-based modeling of host-pathogen systems: The successes and challenges. *Information Sciences*, 179(10): 1379–1389, Apr. 2009. ISSN 0020-0255. doi: 10.1016/j.ins.2008.11.012. URL `https://www.ncbi.nlm.nih.gov/pmc/articles/PMC2731970/`.

C. Beauchemin, J. Samuel, and J. Tuszynski. A simple cellular automaton model for influenza A viral infections. *J. Theor. Biol.*, 232(2):223–234, Jan. 2005. ISSN 00225193. doi: 10.1016/j.jtbi.2004.08.001. URL `https://linkinghub.elsevier.com/retrieve/pii/S0022519304003819`.

C. Beauchemin, N. Dixit, and A. S. Perelson. Characterizing T cell movement within lymph nodes in the absence of antigen. *J. Immunol.*, 178(9):5505–5512, 1 May 2007. URL `http://www.jimmunol.org/cgi/content/abstract/178/9/5505`.

C. A. Beauchemin, J. J. McSharry, G. L. Drusano, J. T. Nguyen, G. T. Went, R. M. Ribeiro, and A. S. Perelson. Modeling amantadine treatment of influenza A virus in vitro. *J. Theor. Biol.*, 254:439–451, 21 September 2008. doi: 10.1016/j.jtbi.2008.05.031.

C. A. Beauchemin, T. Miura, and S. Iwami. Duration of SHIV production by infected cells is not exponentially distributed: Implications for estimates of infection parameters and antiviral efficacy. *Sci. Rep.*, 7:42765, 16 February 2017. doi: 10.1038/srep42765.

R. Bermejo and L. Saavedra. Lagrange-Galerkin methods for the incompressible Navier-Stokes equations: a review. *Comm. Appl. Ind. Math.*, 7(3):23–52, September 2016. doi: 10.1515/caim-2016-0021.

K. Blahut, C. Quirouette, J. J. Feld, S. Iwami, and C. A. A. Beauchemin. Quantifying the relative contribution of free virus and cell-to-cell transmission routes to the propagation of hepatitis C virus infections in vitro using an agent-based model. *arXiv*, February 2021. doi: arXiv:2102.05531.

A. Borghesi, A. Zigliani, R. Masciullo, S. Golemi, P. Maculotti, D. Farina, and R. Maroldi. Radiographic severity index in COVID-19 pneumonia: relationship to age and sex in 783 Italian patients. *Radiol. Medica*, 125(5):461–464, May 2020. doi: 10.1007/s11547-020-01202-1.

L. Bourouiba. Turbulent gas clouds and respiratory pathogen emissions: Potential implications for reducing transmission of COVID-19. *JAMA*, 323(18):1837–1838, May 2020. doi: 10.1001/jama.2020.4756.

B. R. Brückner and A. Janshoff. Importance of integrity of cell-cell junctions for the mechanics of confluent MDCK II cells. *Scientific Reports*, 8(1):14117, Dec. 2018. ISSN 2045-2322. doi: 10.1038/s41598-018-32421-2. URL `http://www.nature.com/articles/s41598-018-32421-2`.

N. Chen, M. Zhou, X. Dong, J. Qu, F. Gong, Y. Han, Y. Qiu, J. Wang, Y. Liu, Y. Wei, J. Xia, T. Yu, X. Zhang, and L. Zhang. Epidemiological and clinical characteristics of 99 cases of 2019 novel coronavirus pneumonia in Wuhan, China: a descriptive study. *Lancet*, 395(10223):507–513, February 15 2020. doi: 10.1016/S0140-6736(20)30211-7.

F. Chiacchio, M. Pennisi, G. Russo, S. Motta, and F. Pappalardo. Agent-based modeling of the immune system: Netlogo, a promising framework. *Biomed Res. Intl.*, 2014: 907171, 2014. doi: 10.1155/2014/907171.

P. Czuppon, F. Debarre, A. Goncalves, O. Tenaillon, A. S. Perelson, J. Guedj, and F. Blanquart. Success of prophylactic antiviral therapy for SARS-CoV-2: Predicted critical efficacies and impact of different drug-specific mechanisms of action. *PLoS Comput. Biol.*, 17(3):1–19, March 1 2021. doi: 10.1371/journal.pcbi.1008752.

H. M. Dobrovolny and C. A. Beauchemin. Modelling the emergence of influenza drug resistance: The roles of surface proteins, the immune response and antiviral mechanisms. *PLoS One*, 12(7):e0180582, 10 July 2017. doi: 10.1371/journal.pone.0180582.

H. M. Dobrovolny, M. J. Baron, R. Gieschke, B. E. Davies, N. L. Jumbe, and C. A. A. Beauchemin. Exploring cell tropism as a possible contributor to influenza infection severity. *PLoS ONE*, 5(11):e13811, November 2010. doi: 10.1371/journal.pone.0013811.

H. M. Dobrovolny, M. B. Reddy, M. A. Kamal, C. R. Rayner, and C. A. Beauchemin. Assessing mathematical models of influenza infections using features of the immune response. *PLoS One*, 8(2):e57088, 28 February 2013. doi: 10.1371/journal.pone.0057088.

M. G. Dodds, R. Krishna, A. Goncalves, and C. R. Rayner. Modelinformed drug repurposing: Viral kinetic modelling to prioritize rational drug combinations for COVID19. *Br. J. Clin. Pharmacol.*, pages 1–12, July 2020. doi: 10.1111/bcp.14486.

P. Dogra, J. Ruiz-Ramrez, K. Sinha, J. D. Butner, M. J. Pelaez, M. Rawat, V. K. Yellepeddi, R. Pasqualini, W. Arap, H. D. Sostman, V. Cristini, and Z. Wang. Innate immunity plays a key role in controlling viral load in COVID-19: mechanistic insights from a whole-body infection dynamics model. *ACS Pharmacol.*, 3(1):248–265, December 30 2020. doi: 10.1021/acsptsci.0c00183.

K. Ejima, K. S. Kim, S. Iwanami, Y. Fujita, M. Li, R. S. Zoh, K. Aihara, T. Miyazaki, T. Wakita, and S. Iwami. Time variation in the probability of failing to detect a case of polymerase chain reaction testing for SARS-CoV-2 as estimated from a viral dynamics model. *J. R. Soc. Interface*, 18:20200947, April 2021. doi: 10.1098/rsif.2020.0947.

M. Gallagher, C. Brooke, R. Ke, and K. Koelle. Causes and Consequences of Spatial Within-Host Viral Spread. *Viruses*, 10(11):627, Nov. 2018. ISSN 1999-4915. doi: 10.3390/v10110627. URL `http://www.mdpi.com/1999-4915/10/11/627`.

M. Gandhi, C. Beyrer, and E. Goosby. Masks do more than protect others during COVID-19: Reducing the inoculum of SARS-CoV-2 to protect the wearer. *J. Gen. Intern. Med.*, 35(10):3063–3066, July 31 2020. doi: 10.1007/s11606-020-06067-8.

M. Gardner. Fantastic combinations of John Conway's new solitaire game of life. *Sci. Am.*, 223(4):120, 1970. doi: 10.1038/scientificamerican1070-120.

M. Getz, Y. Wang, G. An, M. Asthana, A. Becker, C. Cockrell, N. Collier, M. Craig, C. L. Davis, J. R. Faeder, A. N. F. Versypt, T. Mapder, J. F. Gianlupi, J. A. Glazier, S. Hamis, R. Heiland, T. Hillen, D. Hou, M. A. Islam, A. L. Jenner, F. Kurtoglu, C. I. Larkin, B. Liu, F. Macfarlane, P. Maygrundter, P. A. Morel, A. Narayanan, J. Ozik, E. Pienaar, P. Rangamani, A. S. Saglam, J. E. Shoemaker, A. M. Smith, J. J. Weaver, and P. Macklin. Iterative community-driven development of a SARS-CoV-2 tissue simulator. *BioRXiv*, April 2021. doi: 10.1101/2020.04.02.019075.

H. Ginsberg and F. Horsfall. Quantitative aspects of the multiplication of influenza A virus in the mouse lung — relation between the degree of viral multiplication and the extent of pneumonia. *J. Exp. Med.*, 95(2):135–145, 1952. doi: 10.1084/jem.95.2.135.

N. Go, C. Belloc, C. Bidot, and S. Touzeau. Why, when and how should exposure be considered at the within-host scale? a modelling contribution to PRRSv infection. *Math. Med. Biol.*, 36(2):179–206, June 2019. doi: 10.1093/imammb/dqy005.

A. Gonçalves, J. Bertrand, R. Ke, E. Comets, X. de Lamballerie, D. Malvy, A. Pizzorno, O. Terrier, M. R. Calatrava, F. Mentré, P. Smith, A. S. Perelson, and J. Guedj. Timing of antiviral treatment initiation is critical to reduce SARS-CoV-2 viral load. *CPT Pharmacometrics Syst Pharmacol.*, 9(9):509–514, September 2020. doi: 10.1002/psp4.12543.

G. González-Parra and H. M. Dobrovolny. The rate of viral transfer between upper and lower respiratory tracts determines RSV illness duration. *J. Math. Biol.*, 79:467–483, 2019. doi: 10.1007/s00285-019-01364-1.

A. Goyal and J. M. Murray. Modelling the impact of cell-to-cell transmission in hepatitis B virus. *PLoS ONE*, 11(8):e0161978, August 25 2016. doi: 10.1371/journal.pone.0161978.

P. Goyal, J. J. Choi, L. C. Pinheiro, E. J. Schenck, R. Chen, A. Jabri, M. J. Satlin, T. R. Campion, M. Nahid, J. B. Ringel, K. L. Hoffman, M. N. Alshak, H. A. Li, G. T. Wehmeyer, M. Rajan, E. Reshetnyak, N. Hupert, E. M. Horn, F. J. Martinez, R. M. Gulick, and M. M. Safford. Clinical characteristics of Covid-19 in New York City. *N. Engl. J. Med.*, 17 April 2020. doi: 10.1128/JVI.00689-10.

F. Graw, D. N. Martin, A. S. Perelson, S. L. Uprichard, and H. Dahari. Quantification of hepatitis C virus cell-to-cell spread using a stochastic modeling approach. *J. Virol.*, 89(13):6551–6561, July 2015. doi: 10.1128/JVI.00016-15.

M. P. Guallar, R. Meirino, C. Donat-Vargas, O. Corral, N. Jouve, and V. Soriano. Inoculum at the time of SARS-CoV-2 exposure and risk of disease severity. *Intl. J. Infect. Dis.*, 97:290–292, August 2020. doi: 10.1016/j.ijid.2020.06.035.

A. Handel, I. M. Longini, and R. Antia. Antiviral resistance and the control of pandemic influenza: The roles of stochasticity, evolution and model details. *J Theor. Biol.*, 256:117–125, 2009. doi: 10.1016/j.jtbi.2008.09.021.

F. Hayden, L. Jennings, R. Robson, G. Schiff, H. Jackson, B. Rana, G. McClelland, D. Ipe, N. Roberts, and P. Ward. Oral oseltamivir in human experimental influenza b infection. *Antivir. Ther.*, 5(3):205–213, September 2000.

W. He, G. Y. Yi, and Y. Zhu. Estimation of the basic reproduction number, average incubation time, asymptomatic infection rate, and case fatality rate for COVID-19: Meta-analysis and sensitivity analysis. *J. Med. Virol.*, 92(11):2543–2550, June 2020. doi: 10.1002/jmv.26041.

E. A. Hernandez-Vargas and J. X. Velasco-Hernandez. In-host modelling of COVID-19 kinetics in humans. *medRxiv*, March 2020. doi: 10.1101/2020.03.26.20044487.

B. P. Holder, L. E. Liao, P. Simon, G. Boivin, and C. A. A. Beauchemin. Design considerations in building in silico equivalents of common experimental influenza virus assays and the benefits of such an approach. *Autoimmunity*, 44(4), June 2011a. doi: 10.3109/08916934.2011.523267.

B. P. Holder, P. Simon, L. E. Liao, Y. Abed, X. Bouhy, C. A. Beauchemin, and G. Boivin. Assessing the in vitro fitness of an oseltamivir-resistant seasonal A/H1N1 influenza strain using a mathematical model. *PLOS One*, 6(3):e14767, 2011b. doi: 10.1371/journal.pone.0014767.

T. Iida and F. Bang. Infection of the upper respiratory tract of mice with influenza A virus. *Amer. J. Hygiene*, 77(2):169–176, 1963. doi: 10.1093/oxfordjournals.aje.a120306.

P. C. Ilie, S. Stefanescu, and L. Smith. The role of vitamin D in the prevention of coronavirus disease 2019 infection and mortality. *Aging Clin. Exp. Res.*, 32(7):1195–1198, May 2020. doi: 10.1007/s40520-020-01570-8.

J. Itakura, M. Kurosaki, Y. Itakura, S. Maekawa, Y. Asahina, N. Izumi, and N. Enomoto. Reproducibility and usability of chronic virus infection model using agent-based simulation; comparing with a mathematical model. *Biosys.*, 99(1):70–78, January 2010. doi: 10.1016/j.biosystems.2009.09.001.

S. Iwami, J. S. Takeuchi, S. Nakaoka, F. Mammano, F. Clavel, H. Inaba, T. Kobayashi, N. Misawa, K. Aihara, Y. Koyanagi, and K. Sato. Cell-to-cell infection by HIV contributes over half of virus infection. *eLife*, 4:e08150, October 6 2015. doi: 10.7554/eLife.08150.

B. Jessie and H. M. Dobrovolny. The role of syncytia during viral infections. *J. Theor. Biol.*, 525:110749, May 5 2021. doi: 10.1016/j.jtbi.2021.110749.

F. Jiang, L. Deng, L. Zhang, Y. Cai, C. W. Cheung, and Z. Xia. Review of the clinical characteristics of coronavirus disease 2019 (COVID-19). *J. Gen. Intern. Med.*, March 2020. doi: 10.1007/s11606-020-05762-w.

Y. Kakizoe, S. Nakaoka, C. A. Beauchemin, S. Morita, H. Mori, T. Igarashi, K. Aihara, T. Miura, and S. Iwami. A method to determine the duration of the eclipse phase for in vitro infection with a highly pathogenic SHIV strain. *Sci. Rep.*, 5:10371, 21 May 2015. doi: 10.1038/srep10371.

T. Kano, K. Yasui, T. Mikami, M. Asally, and A. Ishiguro. An agent-based model of the interrelation between the COVID-19 outbreak and economic activities. *Proc. Royal Soc. A*, 477(2245):20200604, January 27 2021. doi: 10.1098/rspa.2020.0604.

C. Kerepesi, T. Bakacs, and T. Szabados. MiStImm: an agent-based simulation tool to study the self-nonself discrimination of the adaptive immune response. *Theor. Biol. Math. Model.*, 16:9, May 2 2019. doi: 10.1186/s12976-019-0105-5.

P. Kim and D. Kim. Convergence and stability of a BSLM for advection-diffusion models with Dirichlet boundary conditions. *Appl. Math. Comput.*, 366:124744, February 2020. doi: 10.1016/j.amc.2019.124744.

N. L. Komarova and D. Wodarz. Virus dynamics in the presence of synaptic transmission. *Math. Biosci.*, 242(2):161–171, April 2013. doi: 10.1016/j.mbs.2013.01.003.

P. Kumberger, K. Durso-Cain, S. L. Uprichard, H. Dahari, and F. Graw. Accounting for space - quantification of cell-to-cell transmission kinetics using virus dynamics models. *Viruses*, 10(4):200, April 2018. doi: 10.3390/v10040200.

D. LaBarre and R. Lowy. Improvements in methods for calculating virus titer estimates from $TCID_{50}$ and plaque assays. *J. Virol. Meth.*, 96(2):107–126, August 2001. doi: 10.1016/S0166-0934(01)00316-0.

R. Laubenbacher, J. P. Sluka, and J. A. Glazier. Using digital twins in viral infection. *Science*, 371(6534):1105–1106, March 12 2021. doi: 10.1126/science.abf3370.

D. Levin, S. Forrest, S. Banerjee, C. Clay, J. Cannon, M. Moses, and F. Koster. A spatial model of the efficiency of T cell search in the influenza-infected lung. *J. Theor. Biol.*, 398:52–63, June 7 2016. doi: 10.1016/j.jtbi.2016.02.022.

R. Li, S. Pei, B. Chen, Y. Song, T. Zhang, W. Yang, and J. Shaman. Substantial undocumented infection facilitates the rapid dissemination of novel coronavirus (SARS-CoV2). *Science*, March 2020. doi: 10.1126/science.abb3221.

T. Li, Z. Cheng, and L. Zhang. Developing a novel parameter estimation method for agent-based model in immune system simulation under the framework of history matching: A case study on influenza A virus infection. *Intl. J. Mol. Sci.*, 18(12):2592, December 2017. doi: 10.3390/ijms18122592.

Y. Li and A. Handel. Modeling inoculum dose dependent patterns of acute virus infections. *J. Theor. Biol.*, 347:63–73, April 21 2014. doi: 10.1016/j.jtbi.2014.01.008.

P. Little, R. C. Read, R. Amlôt, T. Chadborn, C. Rice, J. Bostock, Lucy, and Yardley. Reducing risks from coronavirus transmission in the home — the role of viral load. *Brit. Med. J.*, 369:m1728, May 6 2020. doi: 10.1136/bmj.m1728.

J. Liu, S. Li, J. Liu, B. Liang, X. Wang, H. Wang, W. Li, Q. Tong, J. Yi, L. Zhao, L. Xiong, C. Guo, J. Tian, J. Luo, J. Yao, R. Pang, H. Shen, C. Peng, T. Liu, Q. Zhang, J. Wu, L. Xu, S. Lu, B. Wang, Z. Weng, C. Han, H. Zhu, R. Zhou, H. Zhou, X. Chen, P. Ye, B. Zhu, L. Wang, W. Zhou, S. He, Y. He, S. Jie, P. Wei, J. Zhang, Y. Lu, W. Wang, L. Zhang, L. Li, F. Zhou, J. Wang, U. Dittmer, M. Lu, Y. Hu, D. Yang, and X. Zheng. Longitudinal characteristics of lymphocyte responses and cytokine profiles in the peripheral blood of SARS-CoV-2 infected patients. *EBiomed.*, 55:UNSP 102763, May 2020a. doi: 10.1016/j.ebiom.2020.102763.

Y. Liu, W. Liao, L. Wan, T. Xiang, and W. Zhang. Correlation between relative nasopharyngeal virus RNA load and lymphocyte count disease severity in patients with COVID-19. *Viral Immunol.*, 34(5):330–335, April 2020b. doi: 10.1089/vim.2020.0062.

H. Manchanda, N. Seidel, A. Krumbholz, A. Sauerbrei, M. Schmidtke, and R. Guthke. Within-host influenza dynamics: A small-scale mathematical modeling approach. *Biosystems*, 118:51–59, April 2014. doi: 10.1016/j.biosystems.2014.02.004.

B. Manicassamy, S. Manicassamy, A. Belicha-Villanueva, G. Pisanelli, B. Pulendran, and A. Garca-Sastre. Analysis of in vivo dynamics of influenza virus infection in mice using a GFP reporter virus. *Proc. Natl. Acad. Sci. U.S.A.*, 107(25):11531–11536, 22 June 2010. doi: 10.1073/pnas.0914994107.

R. Mittal, R. Ni, and J.-H. Seo. The flow physics of COVID-19. *J. Fluid Phys.*, 894:F2, July 10 2020. doi: 10.1017/jfm.2020.330.

J. R. Moore, H. Ahmed, B. Manicassamy, A. Garcia-Sastre, A. Handel, and R. Antia. Varying inoculum dose to assess the roles of the immune response and target cell depletion by the pathogen in control of acute viral infections. *Bulletin of Mathematical Biology*, 82(3):UNSP 35, March 3 2020. doi: 10.1007/s11538-020-00711-4.

L. Morawska and J. Cao. Airborne transmission of SARS-CoV-2: The world should face the reality. *Env. Intl.*, 139:105730, June 2020. doi: 10.1016/j.envint.2020.105730.

C. N. Ngonghala, E. Iboi, S. Eikenberry, M. Scotch, C. R. MacIntyre, M. H. Bonds, and A. B. Gumel. Mathematical assessment of the impact of non-pharmaceutical interventions on curtailing the 2019 novel coronavirus. *Math. Biosci.*, 325:108364, July 2020. doi: 10.1016/j.mbs.2020.108364.

D. D. Nogare and A. B. Chitnis. Netlogo agent-based models as tools for understanding the self-organization of cell fate, morphogenesis and collective migration of the zebrafish posterior lateral line primordium. *Seminars Cell Develop. Biol.*, 100:186–198, April 2020. doi: 10.1016/j.semcdb.2019.12.015.

N. Nant, G. Lingas, Q. Le Hingrat, Jade Ghosn, Ilka Engelmann, Quentin Lepiller, A. Gaymard, V. Ferre, C. Hartard, J.-C. Plantier, V. Thibault, J. Marlet, B. Montes, K. Bouiller, F.-X. Lescure, J.-F. Timsit, E. Faure, J. Poissy, C. Chidiac, F. Raffi, A. Kimmoun, M. Etienne, J.-C. Richard, P. Tattevin, D. Garot, V. Le Moing, D. Bachelet, C. Tardivon, X. Duval, Y. Yazdanpanah, F. Mentré, C. Laouénan, B. Visseaux, and J. Guedj. Modeling SARS-CoV-2 viral kinetics and association with mortality in hospitalized patients from the French COVID cohort. *Proc. Natl. Acad. Sci. U.S.A.*, 18(8):e2017962118, January 2021. doi: 10.1073/pnas.2017962118.

D. L. Olsen-Kettle. Numerical solution of partial dierential equations. page 108.

OpenStax, N. Parker, M. Schneegurt, A.-H. T. Tu, B. Forster, and P. Lister. Microbiology. *Open Educational Resources Collection*, Nov. 2016. URL `https://irl.umsl.edu/oer/3`.

M. Ottolini, D. Porter, V. Hemming, S. Hensen, I. Sami, and G. Prince. Semi-permissive replication and functional aspects of the immune response in a cotton rat model of human parainfluenza virus type 3 infection. *J. Gen. Virol.*, 77(8):1739–1743, August 1996. doi: 10.1099/0022-1317-77-8-1739.

M. Ottolini, J. Blanco, M. Eichelberger, D. Porter, L. Pletneva, J. Richardson, and G. Prince. The cotton rat provides a useful small-animal model for the study of influenza virus pathogenesis. *J. Gen. Virol.*, 86(10):2823–2830, October 2005. doi: 10.1099/vir.0.81145-0.

K. A. Owusu, E. Acevedo-Trejos, M. M. Fall, and A. Merico. Effects of cooperation and different characteristics of marine protected areas in a simulated small-scale fishery. *Ecol. Complex.*, 44:100876, December 2020. doi: 10.1016/j.ecocom.2020.100876.

K. Pankaj. Virus Identification and Quantification. *Materials and Methods*, June 2021. URL `https://www.labome.com/method/Virus-Identification-and-Quantification.html`.

A. C. Paulo, M. Correia-Neves, T. Domingos, A. G. Murta, and J. Pedrosa. Influenza infectious dose may explain the high mortality of the second and third wave of 19181919 influenza pandemic. *PLoS ONE*, 5(7):e11655, July 27 2010. doi: 0.1371/journal.pone.0011655.

L. T. Pinilla, B. P. Holder, Y. Abed, G. Boivin, and C. A. A. Beauchemin. The H275Y neuraminidase mutation of the pandemic A/H1N1 influenza virus lengthens the eclipse phase and reduces viral output of infected cells, potentially compromising fitness in ferrets. *J. Virol.*, 86(19):10651–10660, October 2012. doi: 10.1128/JVI.07244-11.

I. Price, E. D. Mochan-Keef, D. Swigon, B. G. Ermentrout, S. Lukens, F. R. Toapanta, T. M. Ross, and G. Clermont. The inflammatory response to influenza A virus (H1N1): An experimental and mathematical study. *Phys. Rev. Lett.*, 374:83–93, 15 June 2015. doi: 10.1016/j.jtbi.2015.03.017.

G. Prince, D. Porter, A. Jenson, R. Horswood, R. Chanock, and H. Ginsberg. Pathogenesis of adenovirus type-5 pneumonia in cotton rats (sigmodon-hispidus). *J. Virol.*, 67 (1):101–111, January 1993. doi: 10.1128/JVI.67.1.101-111.1993.

C. Quirouette, N. P. Younis, M. B. Reddy, and C. A. A. Beauchemin. A mathematical model describing the localization and spread of influenza A virus infection within the human respiratory tract. *PLoS Comput. Biol.*, 16(4):e1007705, April 13 2020. doi: 10.1371/journal.pcbi.1007705.

M. N. Read, K. Alden, L. M. Rose, and J. Timmis. Automated multi-objective calibration of biological agent-based simulations. *J. R. Soc. Interface*, 13(122):20160543, September 1 2016. doi: 10.1098/rsif.2016.0543.

K. Sneppen, B. F. Nielsen, R. J. Taylor, and L. Simonsen. Overdispersion in COVID-19 increases the effectiveness of limiting nonrepetitive contacts for transmission control.

Proc. Natl. Acad. Sci. U.S.A., 118(14):e2016623118, April 6 2021. doi: 10.1073/pnas.2016623118.

L. Sun, L. Shen, J. Fan, F. Gu, M. Hu, Y. An, Q. Zhou, H. Fan, and J. Bi. Clinical features of patients with coronavirus disease 2019 from a designated hospital in Beijing, China. *J. Med. Virol.*, June 2020. doi: 10.1002/jmv.25966.

Thermofisher. Useful Numbers for Cell Culture - US. `https://www.thermofisher.com/us/en/home/references/gibco-cell-culture-basics/cell-culture-protocols/cell-culture-useful-numbers.html`. Library Catalog: www.thermofisher.com.

A. Timm and J. Yin. Kinetics of virus production from single cells. *Virol.*, 424:11–17, 4 January 2012. doi: 10.1016/j.virol.2011.12.005.

X. Tong, J. Chen, H. Miao, T. Li, and L. Zhang. Development of an Agent-Based Model (ABM) to Simulate the Immune System and Integration of a Regression Method to Estimate the Key ABM Parameters by Fitting the Experimental Data. *PLOS ONE*, 10 (11):e0141295, Nov. 2015. ISSN 1932-6203. doi: 10.1371/journal.pone.0141295. URL `https://dx.plos.org/10.1371/journal.pone.0141295`.

L. Wang, X. Fan, G. Bonenfant, D. Cui, J. Hossain, N. Jiang, G. Larson, M. Currier, J. Liddell, M. Wilson, A. Tamin, J. Harcourt, J. Ciomperlik-Patton, H. Pang, N. Dybdahl-Sissoko, R. Campagnoli, P.-Y. Shi, J. Barnes, N. J. Thornburg, D. E. Wentworth, and B. Zhou. Susceptibility to SARS-CoV-2 of Cell Lines and Substrates Commonly Used to Diagnose and Isolate Influenza and Other Viruses. *Emerging Infectious Diseases*, 27(5):1380–1392, May 2021. ISSN 1080-6040, 1080-6059. doi: 10.3201/eid2705.210023. URL `https://wwwnc.cdc.gov/eid/article/27/5/21-0023_article.htm`.

S. Wang, Y. Pan, Q. Wang, H. Miao, A. N. Brown, and L. Rong. Modeling the viral dynamics of SARS-CoV-2 infection. *Math. Biosci.*, 328:108438, October 2020. doi: 10.1016/j.mbs.2020.108438.

S. Wasik, P. Jackowiak, M. Figlerowicz, and J. Blazewicz. Multi-agent model of hepatitis C virus infection. *Arti. Intel. Med.*, 60(2):123–131, February 2014. doi: 10.1016/j.artmed.2013.11.001.

WebPlotDigitizer. WebPlotDigitizer - Extract data from plots, images, and maps. https://automeris.io/WebPlotDigitizer/.

B. Wendroff. Difference Methods for Initial-Value Problems (Robert D. Richtmyer and K. W. Morton). *SIAM Review*, 10(3):381–383, July 1968. ISSN 0036-1445. doi: 10.1137/1010073. URL `https://epubs.siam.org/doi/abs/10.1137/1010073`. Publisher: Society for Industrial and Applied Mathematics.

D. Wethington, O. Harder, K. Uppulury, W. C. Stewart, P. Chen, T. King, S. D. Reynolds, A. S. Perelson, M. E. Peeples, S. Niewiesk, and J. Das. Mathematical

modelling identifies the role of adaptive immunity as a key controller of respiratory syncytial virus in cotton rats. *J. Roy. Soc. Interface*, 16(160):20190389, November 2019. doi: 10.1098/rsif.2019.0389.

J. Whitman, A. Dhanji, F. Hayot, S. C. Sealfon, and C. Jayaprakash. Spatio-temporal dynamics of host-virus competition: A model study of influenza A. *J. Theor. Biol.*, 484:110026, January 7 2020. doi: 10.1016/j.jtbi.2019.110026.

D. Wodarz, C. N. Chan, B. Trinite, N. L. Komarova, and D. N. Levy. On the Laws of Virus Spread through Cell Populations. *Journal of Virology*, 88(22):13240–13248, Nov. 2014. ISSN 0022-538X, 1098-5514. doi: 10.1128/JVI.02096-14. URL `https://jvi.asm.org/content/88/22/13240`.

F. Wu, S. Zhao, B. Yu, Y.-M. Chen, W. Wang, Z.-G. Song, Y. Hu, Z.-W. Tao, J.-H. Tian, Y.-Y. Pei, M.-L. Yuan, Y.-L. Zhang, F.-H. Dai, Y. Liu, Q.-M. Wang, J.-J. Zheng, L. Xu, E. C. Holmes, and Y.-Z. Zhang. A new coronavirus associated with human respiratory disease in China. *Nature*, 579(7798):265–271, March 2020. doi: 10.1038/s41586-020-2008-3.

Q. Xu and H. An. A class of domain decomposition based nonlinear explicit-implicit iteration algorithms for solving diffusion equations with discontinuous coefficient. *J. Comp. Appl. Math.*, 386:113232, April 2021. doi: 10.1016/j.cam.2020.113232.

X. Xu. Update: Influenza Activity in the United States During the 201819 Season and Composition of the 201920 Influenza Vaccine. *MMWR. Morbidity and Mortality Weekly Report*, 68, 2019. ISSN 0149-21951545-861X. doi: 10.15585/mmwr.mm6824a3. URL `https://www.cdc.gov/mmwr/volumes/68/wr/mm6824a3.htm`.

Y. Yang, C. Shen, J. Li, J. Yuan, M. Yang, F. Wang, G. Li, Y. Li, L. Xing, L. Peng, J. Wei, M. Cao, H. Zheng, W. Wu, R. Zou, D. Li, Z. Xu, H. Wang, M. Zhang, Z. Zhang, L. Liu, and Y. Liu. Exuberant elevation of IP-10, MCP-3 and IL-1ra during SARS-CoV-2 infection is associated with disease severity and fatal outcome. *J. Allergy Clin. Immunol.*, 146(1):119–127, April 29 2020. doi: 10.1016/j.jaci.2020.04.027.

F. Ying and N. O'Clery. Modelling COVID-19 transmission in supermarkets using an agent-based model. *PLoS ONE*, 16(4):e0249821, April 9 2021. doi: 10.1371/journal.pone.0249821.

J. Zhang, X. Dong, Y. Cao, Y. Yuan, Y. Yang, Y. Yan, C. A. Akdis, and Y. Gao. Clinical characteristics of 140 patients infected with SARSCoV2 in Wuhan, China. *Allergy*, 75 (7):1730–1741, February 27 2020. doi: 10.1111/all.14238.

J. Zheng and S. Perlman. Immune responses in influenza A virus and human coronavirus infections: an ongoing battle between the virus and host. *Curr. Opin. Virol.*, 28:43–52, February 2018. doi: 10.1016/j.coviro.2017.11.002.

VITA

Personal Background	Baylor G. Fain Raised in Texas Son of Sharon E. Fain & *the late* Gary G. Fain Spouse: Kelli R. Gill
Awards	BSA Heroism Award, Awarded for water rescue, Canton, Texas, 2011 Eagle Scout, Project: Bridge construction at Cherry Creek Park, Canton, Texas, 2011
Education	Diploma, Canton High School, Canton, Texas, 2012 Bachelor of Science, Physics, Tarleton State University, Stephenville, Texas, 2016
Experience	Undergraduate Research Assistant, Texas A&M University, College Station, Texas, May 2014-August 2014 Research Assistant, Tarleton State University, Stephenville, Texas, May 2015-May 2016 Teaching Assistantship, Texas Christian University, Fort Worth, Texas, 2018-2021
Research Awards	Research Grant, SERC Grant, Texas Christian University, Forth Worth, Texas, 2019 Best Poster, SIAM TX-LA, Southern Methodist University, Dallas, Texas, 2019 Best Poster, Society for Mathematical Biology, Virtual, 2020

Publications

1. B.M. Wyatt, [et al., including **Fain, B.**], 2018, "Creating an Isotopically Similar Earth-Moon System with Correct Angular Momentum from a Giant Impact," Journal of Astrophysics and Astronomy **39**:26. Times cited: 3.

2. **Fain, B.**, H.M. Dobrovolny, 2020, "Initial Inoculum and the Severity of COVID-19: A Mathematical Modeling Study of the Dose-Response of SARS-CoV-2 Infections," Epidemiologia **1**:5-15. Times cited: 5.

3. **Fain, B.**, H.M. Dobrovolny, "GPU acceleration and data fitting: Agent-based models of viral infections can now be parameterized in hours," submitted to Journal of Computational Science.

ABSTRACT

APPLYING DESKTOP GPUS TO A HYBRID ABM AND PDM: MODEL VALIDATION AND RAPID SIMULATION OF VIRAL INFECTIONS

by Baylor G. Fain, Ph.D., 2021
Department of Physics and Astronomy
Texas Christian University

Major Advisor, Dr. Hana Dobrovolny, Associate Professor of Biophysics

For many years, infectious disease modelers have used agent-based models to study the spread of viruses, but the models were too computationally intensive to fully replicate even in vitro experiments. Now, with technological advancements and accessible software, agent-based models can be used to their full potential. This thesis shows an agent-based model that expresses viral transmission and diffusion, can manipulate and track individual cells, and can be fit to real experimental data in a timely manner due to acceleration of computation with graphics processing units (GPUs). The use of GPUs allows simulations to run on desktop computers in a few seconds or minutes, while still simulating an accurate number of cells to replicate *in vitro* viral infection experiments. This model can now be used to study in-host infections quickly, so that in the event of an outbreak or epidemic a treatment plan and course of action can be developed in less time.